GEOPHYSICS, VOL. 80, NO. 1 (JANUARY-FEBRUARY 2015); P. G35–G51, 18 FIGS., 2 TABLES.
10.1190/GEO2014-0188.1

A local level-set method for 3D inversion of gravity-gradient data

Wangtao Lu[1] and Jianliang Qian[1]

ABSTRACT

We have developed a local level-set method for inverting 3D gravity-gradient data. To alleviate the inherent nonuniqueness of the inverse gradiometry problem, we assumed that a homogeneous density contrast distribution with the value of the density contrast specified a priori was supported on an unknown bounded domain D so that we may convert the original inverse problem into a domain inverse problem. Because the unknown domain D may take a variety of shapes, we parametrized the domain D by a level-set function implicitly so that the domain inverse problem was reduced to a nonlinear optimization problem for the level-set function. Because the convergence of the level-set algorithm relied heavily on initializing the level-set function to enclose the gravity center of a source body, we applied a weighted L^1-regularization method to locate such a gravity center so that the level-set function can be properly initialized. To rapidly compute the gradient of the nonlinear functional arising in the level-set formulation, we made use of the fact that the Laplacian kernel in the gravity force relation decayed rapidly off the diagonal so that matrix-vector multiplications for evaluating the gradient can be accelerated significantly. We conducted extensive numerical experiments to test the performance and effectiveness of the new method.

INTRODUCTION

Gravity gradiometry measures the gravity-gradient tensor, consisting of the gradient of each component of the gravity field, at or above the ground surface of the earth. Modern gradiometry instruments, such as the full tensor gravity (FTG) system and the airborne FALCON system, measure (directly or indirectly) the differential curvature and the gradient of the vertical component of the gradient of the potential field (Pilkington, 2012) because the gravity-gradient tensor contains only five independent components. Interpretation of gravity-gradient data is one of the most significant tasks in geologic sciences because such interpretation can help to analyze the composition of the earth and target subsurface source bodies, such as mineral deposits and so on. Because recently developed airborne systems can collect the gravity-related data in much larger areas more quickly and cheaply than traditional ground-based systems, and because the gravity-gradient data are more sensitive to lateral variability of subsurface source bodies and hence can perhaps provide better lateral resolution than gravity data, gravity-gradient data have become more attractive in practical surveys nowadays. However, because gravity-gradient data are higher order derivatives of the potential, manual interpretation of such data is extremely challenging whereas automatic interpretation calls for developing efficient inversion methods.

Many techniques (Last and Kubik, 1983; Li and Oldenburg, 1998; Condi and Talwani, 1999; Portniaguine and Zhdanov, 1999; Jorgensen and Kisabeth, 2000; Li, 2001a, 2001b; Routh et al., 2001; Zhdanov et al., 2004; Krahenbuhl and Li, 2006; Barnes et al., 2008; Li, 2010; Martinez et al., 2010; Barnes and Barraud, 2012; Martinez et al., 2013) have been developed for the inversion of gravity data or gravity-gradient data during the past decades; a priori geologic information and constraints on density models are usually incorporated in the existing techniques to ensure that the resulting solutions conform to realistic earth models (Last and Kubik, 1983; Li and Oldenburg, 1998; Condi and Talwani, 1999; Portniaguine and Zhdanov, 1999). Meanwhile, fast imaging methods (Fedi and Florio, 2006; Fedi, 2007; Zhdanov et al., 2011; Cella and Fedi, 2012; Fedi and Pilkington, 2012) have also been developed to directly locate the gravity center of a source body. Because most inversion techniques provide quantitative descriptions for subsurface structures, one has to extract the position of a source body from resulting solutions afterward, and this is not an easy task. Therefore, to avoid such indirect extracting procedure, we are motivated to develop a more direct method to delineate subsurface source bodies.

We propose for inverting 3D gravity-gradient data, a local level-set method, which automatically determines positions of source

Manuscript received by the Editor 22 April 2014; revised manuscript received 24 August 2014; published online 2 January 2015.
[1]Michigan State University, Department of Mathematics, East Lansing, Michigan, USA. E-mail: wangtaol@math.msu.edu; qian@math.msu.edu.

bodies. The method is analogous to a recently developed local level-set method for the inversion of gravity data (Isakov et al., 2011, 2013). Mathematically, we formulate the inversion of gravity-gradient data as the following inverse problem: We find the density contrast ρ in a subsurface domain Ω, given the gravity-gradient data on a measurement surface $\Gamma \subset \mathbb{R}^3/\Omega$. To alleviate the inherent nonuniqueness of the inverse gradiometry problem, we assume that a homogeneous density contrast ρ is supported on an unknown bounded domain D of constant density contrast ρ_0, that is, $\rho = \rho_0 \chi_D$, so that we may convert the original inverse problem into a domain inverse problem. Although subsurface source bodies can have arbitrary density distributions, by the equivalent-source principle, there exists an average density contrast ρ_0 and an associated domain D so that the density distribution $\rho = \rho_0 \chi_D$ can reproduce the given gradiometry data. However, one cannot find the value of density contrast ρ_0 and the domain D simultaneously because there may exist infinitely many pairs $\{\rho_0, D\}$ that will reproduce the same gradiometry data. Fortunately, because a priori information on subsurface structures can help to determine ρ_0, we only need to find the domain D.

Because the unknown domain D may have a variety of possible shapes, we introduce a level-set function to parametrize the domain D so that the domain inverse problem is reduced to a nonlinear optimization problem for the level-set function. Because the convergence of the level-set algorithm relies heavily on initializing the level-set function to enclose the gravity center of a source, we apply a weighted L^1-regularization method to locate such a gravity center so that the level-set function can be properly initialized. To rapidly compute the gradient of the nonlinear functional arising in the level-set formulation, we make use of the fact that the Laplacian kernel in the gravity force relation decays rapidly off the diagonal so that matrix-vector multiplications for evaluating the gradient can be accelerated significantly.

The reason we choose the level-set method for the inverse gradiometry problem is the following: For the geometric domain inverse problem under consideration, one needs to deal with closed irregular surfaces that are the boundary of an underlying domain. To describe such an irregular surface, one may introduce some surface parametrization so that one can carry out manipulation on such a surface to fit the given data. However, because such an irregular surface may change shapes or connectivities during the nonlinear data-fitting process, we need to design a reliable and robust parameterization that is capable of changing shapes or connectivities automatically, and the level-set implicit parametrization (Osher and Sethian, 1988) is exactly such a parametrization. We start with a continuous function that is defined everywhere in the whole computational domain, and we further require that this function be positive inside a targeted domain and negative outside, which implies that the zero level-set, in which the function is zero, describes exactly the boundary of the targeted domain, and this function is called the *level-set function*. A level-set implicit parametrization provides many advantages, such as having globally defined functions to manipulate, and the changes of geometry shape and connectivities can be automatically taken care of due to the underlying physical mechanism.

We remark that in the literature, the level-set method (Osher and Sethian, 1988) has been widely used as a suitable and powerful tool for interfaces and shape-optimization problems mainly due to its ability in automatic interface merging and topological changes. In terms of nongeophysical inverse problems, the level-set method is first used for inverse obstacle problems by Santosa (1996); since then, it has been applied to a variety of inverse problems. Litman et al. (1998) use it to reconstruct 2D binary obstacles, and Burger (2001) proposes different choices of descent directions to evolve level-sets for inverse obstacle problems; furthermore, the level-set method was used for inverse scattering problems to reconstruct geometry of extended targets by Hou et al. (2004) and Dorn and Lesselier (2006), for electric resistance tomography in medical imaging by Ben Hadj Miled and Miller (2007), and for piecewise constant surface reconstruction by Van den Doel et al. (2010); see Burger and Osher (2005) for a survey of related applications. In terms of geophysical inverse problems, the level-set method has also found wide applications, and the following citations are by no means complete. Isakov et al. (2011) first apply the level-set method to gravity data; Papadopoulos et al. (2011) apply it to identify uncertainties in the shape of geophysical objects using temperature measurements; Li and Leung (2013), Zheglova et al. (2013), and Li et al. (2014) apply it to traveltime tomography problems in different settings.

The rest of this paper is organized as follows: We start to present the methodology by developing a level-set-based formulation for the inverse gradiometry problem and then address several implementation issues. Numerical experiments are carried out to exhibit performance and effectiveness of the local level-set method.

METHODOLOGY

Inverse gradiometry problem

We begin with the mathematical description of the inverse gradiometry problem. The gravity potential field u satisfies

$$u(\mathbf{r};\rho) = 4\pi\gamma \int_\Omega K(\mathbf{r}, \tilde{\mathbf{r}})\rho(\tilde{\mathbf{r}})d\tilde{\mathbf{r}}, \qquad \mathbf{r} \in \Gamma, \tag{1}$$

where $\Omega \in \mathbb{R}^3$ is a subsurface domain, ρ is the density in Ω, K is Green's function of the 3D Laplace equation,

$$K(\mathbf{r}, \tilde{\mathbf{r}}) = \frac{1}{4\pi|\mathbf{r} - \tilde{\mathbf{r}}|}, \qquad \mathbf{r} \neq \tilde{\mathbf{r}}, \tag{2}$$

where γ is the universal gravitational constant, $\Gamma \subset \mathbb{R}^3/\Omega$ is the measurement surface, $\mathbf{r} = (x, y, z)$ and $\{x, y, z\}$ is the standard Cartesian coordinate system.

Gravity gradiometry measures the gradient of each component of the gravity field on Γ, comprising the following gravity-gradient tensor:

$$\mathbf{T} = \begin{bmatrix} u_{xx} & u_{xy} & u_{xz} \\ u_{yx} & u_{yy} & u_{yz} \\ u_{zx} & u_{zy} & u_{zz} \end{bmatrix}. \tag{3}$$

Because u satisfies the Laplace equation outside Ω and the differential operators are commutative, the gravity tensor $\mathbf{T}$ is symmetric with a zero trace and only five components in $\mathbf{T}$ are linearly independent. Modern gradiometers measure some or all of the following five components: the differential curvature components, namely, u_{xy} and $u_\Delta = (u_{xx} - u_{yy})/2$, and the gradient of the vertical gravity field, namely, u_{zz}, u_{xz}, and u_{yz}. In fact, we have

$$u_s(\mathbf{r};\rho) = 4\pi\gamma \int_\Omega K_s(\mathbf{r},\tilde{\mathbf{r}})\rho(\tilde{\mathbf{r}})d\tilde{\mathbf{r}}, \qquad \mathbf{r} \in \Gamma, \tag{4}$$

for any $s \in \mathbf{M}_{\text{all}} = \{\Delta, xy, zz, xz, yz\}$. Here, K_s denotes the second-order partial derivative of Green's function K with respect to the component indexed by s; in particular,

$$K_\Delta = \frac{1}{2}(\partial_x^2 K - \partial_y^2 K). \tag{5}$$

Normally, we always separate the residual gravity field from the remaining background field so that we only need to analyze the distribution of the density contrast over the remaining background; without confusing, we will overload u and ρ as the residual gravity potential on Γ and the density contrast in Ω, respectively, and we will refer to the residual gravity field as the gravity field in the following. Thus, mathematically, we can formulate the inverse gradiometry problem as follows: Find the density contrast ρ in a subsurface domain Ω, given the gravity-gradient data on the measurement surface $\Gamma \subset \mathbb{R}^3/\Omega$. To alleviate the inherent nonuniqueness of the inverse gradiometry problem, we assume that the homogeneous density contrast ρ in Ω is supported on an unknown bounded domain $D \subset \Omega$, i.e., $\rho = \rho_0\chi_D$, where ρ_0 is a constant. As ρ_0 and D cannot be determined simultaneously, we assume that the density contrast ρ_0 is known in advance. Therefore, the inverse gradiometry problem can be restated: Find the unknown domain $D \subset \Omega$ with a given density contrast ρ_0 that satisfies the following condition:

$$u_s(\mathbf{r};\rho_0\chi_D) = g_s(\mathbf{r}), \quad \text{for } \mathbf{r} \in \Gamma, \tag{6}$$

for s belonging to an index set $\mathbf{M} \subset \mathbf{M}_{\text{all}}$, where $\{g_s\}_{s\in\mathbf{M}}$ are the set of gradient data measured on the surface $\Gamma \subset \mathbb{R}^3/\Omega$.

A level-set-based formulation

Because D may have a variety of possible shapes or connectivities, we propose to parametrize its boundary by a level-set function $\phi^*: \Omega \to \mathbb{R}$, which is continuous and satisfies

$$\begin{aligned} \phi^*(\mathbf{r}) &> 0, \quad \text{for } \mathbf{r} \in D, \\ \phi^*(\mathbf{r}) &= 0, \quad \text{for } \mathbf{r} \in \partial D, \\ \phi^*(\mathbf{r}) &< 0, \quad \text{for } \mathbf{r} \in \bar{D}^c. \end{aligned} \tag{7}$$

Thus, we have for $s \in \mathbf{M}$,

$$\begin{aligned} g_s(\mathbf{r}) = u_s(\mathbf{r};\rho_0\chi_D) &= 4\pi\gamma\rho_0 \int_D K_s(\mathbf{r},\tilde{\mathbf{r}})d\tilde{\mathbf{r}} \\ &= 4\pi\gamma\rho_0 \int_\Omega K_s(\mathbf{r},\tilde{\mathbf{r}})H(\phi^*(\tilde{\mathbf{r}}))d\tilde{\mathbf{r}}, \end{aligned} \tag{8}$$

where H is the Heaviside function defined by

$$H(x) := \begin{cases} 1, & x \geq 0, \\ 0, & \text{otherwise.} \end{cases} \tag{9}$$

For any level-set function $\phi: \Omega \to \mathbb{R}$, we define the forward operator $\mathbf{A}$ as

$$\mathbf{A}(\phi) = [A_s(\phi)]_{s\in\mathbf{M}} \tag{10}$$

and

$$A_s(\phi)(\mathbf{r}) = 4\pi\gamma\rho_0 \int_\Omega K_s(\mathbf{r},\tilde{\mathbf{r}})H(\phi(\tilde{\mathbf{r}}))d\tilde{\mathbf{r}}, \tag{11}$$

where $[A_s]_{s\in\mathbf{M}}$ denotes a column vector of A_s for $s \in \mathbf{M}$.

We solve the following minimizing problem to find ϕ^*:

$$\min J(\phi) = \min \|\mathbf{A}(\phi) - \mathbf{g}\| = \min \sum_{s\in\mathbf{M}} \|G_s(\cdot;\phi)\|^2_{L^2(\Gamma)}, \tag{12}$$

where $\mathbf{g} = [g_s]_{s\in\mathbf{M}}$ and the mismatch term

$$G_s(\mathbf{r};\phi) = A_s(\phi)(\mathbf{r}) - g_s(\mathbf{r}), \tag{13}$$

for $s \in \mathbf{M}$. According to equation 8, $J(\phi)$ attains the minimum at $\phi = \phi^*$.

A necessary condition for ϕ being a minimizer is that the Fréchet derivative of the objective functional J with respect to ϕ is 0. The Fréchet derivative $\partial J/\partial\phi$ is well defined through

$$J(\phi + h) - J(\phi) = \left\langle \frac{\partial J}{\partial \phi}, h \right\rangle + o(\|h\|) \tag{14}$$

for any $h \in L^2(\Omega)$, where $\langle\cdot,\cdot\rangle$ is the standard inner product in $L^2(\Omega)$.

Because

$$\begin{aligned} &J(\phi+h) - J(\phi) = \sum_{s\in\mathbf{M}} \int_\Gamma [G_s(\mathbf{r};\phi+h)^2 - G_s(\mathbf{r};\phi)^2] d\sigma(\mathbf{r}) \\ &= 4\pi\gamma\rho_0 \sum_{s\in\mathbf{M}} \int_\Gamma \left\{ (2G_s(\mathbf{r};\phi) + o(\|h\|)) \int_\Omega K_s(\mathbf{r},\tilde{\mathbf{r}})[H(\phi+h) \right. \\ &\left. - H(\phi)]d\tilde{\mathbf{r}} \right\} d\sigma(\mathbf{r}) \\ &= 4\pi\gamma\rho_0 \sum_{s\in\mathbf{M}} \int_\Gamma \left\{ 2G_s(\mathbf{r};\phi) \int_\Omega K_s(\mathbf{r},\tilde{\mathbf{r}})[\delta(\phi(\tilde{\mathbf{r}}))h(\tilde{\mathbf{r}}) \right. \\ &\left. + o(\|h\|)]d\tilde{\mathbf{r}} \right\} d\sigma(\mathbf{r}) + o(\|h\|) \\ &= \sum_{s\in\mathbf{M}} \int_\Omega \left\{ h(\tilde{\mathbf{r}}) 8\pi\gamma\rho_0 \int_\Gamma G_s(\mathbf{r};\phi)K_s(\mathbf{r},\tilde{\mathbf{r}})d\sigma(\mathbf{r})\delta(\phi(\tilde{\mathbf{r}})) \right\} d\tilde{\mathbf{r}} \\ &+ o(\|h\|), \end{aligned} \tag{15}$$

we obtain

$$\frac{\partial J}{\partial \phi}(\tilde{\mathbf{r}}) = 8\pi\gamma\rho_0 \sum_{s\in\mathbf{M}} \int_\Gamma G_s(\mathbf{r};\phi)K_s(\mathbf{r},\tilde{\mathbf{r}})d\sigma(\mathbf{r})\delta(\phi(\tilde{\mathbf{r}})). \tag{16}$$

Therefore, the necessary condition is simplified to

$$\frac{\partial J}{\partial \phi} = 8\pi\gamma\rho_0 \sum_{s\in\mathbf{M}} \int_\Gamma G_s(\mathbf{r};\phi)^T K_s(\mathbf{r},\tilde{\mathbf{r}}) d\sigma(\mathbf{r}) \delta(\phi(\tilde{\mathbf{r}})) = 0;$$
$$\frac{1}{|\nabla\phi|}\frac{\partial\phi}{\partial\boldsymbol{\nu}} = 0 \quad \text{on } \partial\Omega, \tag{17}$$

where $\boldsymbol{\nu}$ denotes the unit normal vector to $\partial\Omega$ and we impose the natural boundary condition on ϕ so that ϕ does not change rapidly away from Ω. By the method of steepest descent, we end up with the evolution equations

$$\frac{\partial\phi}{\partial t} = -\frac{\partial J}{\partial\phi}; \quad \frac{1}{|\nabla\phi|}\frac{\partial\phi}{\partial\boldsymbol{\nu}} = 0 \quad \text{on } \partial\Omega, \tag{18}$$

where $\phi = \phi(\mathbf{r}, t)$ with t being the artificial evolution time. Therefore, we take the exact solution to be $\phi^* = \phi(\mathbf{r}, \infty)$ and the boundary ∂D to be the zero level set of ϕ^*: $\partial D = \{\mathbf{r}: \phi^*(\mathbf{r}) = 0\}$.

We remark that our level-set-based formulation provides implicit regularization in the evolution process. More specifically, to ensure that the evolution equation guides the level-set function ϕ toward the exact solution ϕ^* stably, we need to reinitialize the level-set function ϕ frequently, so that $|\nabla\phi| = 1$ in Ω and the level-set function ϕ does not change rapidly near interfaces (Sussman et al., 1994); this reinitialization procedure serves as an implicit regularization on the inverse gradiometry problem. Next, the evolution equation requires that the level-set function ϕ be at least differentiable once, which is considered to be another implicit regularization. In addition, the coarseness of discretization of Ω can be considered to be an implicit regularization as well because it may affect the resolution of numerical inversions.

In the following, we take the computational domain Ω to be a rectangular cuboid and the measurement surface Γ to be a planar surface above the top face of Ω.

Numerical implementation

We apply the following level-set algorithm to find D: In the following, we give motivations and details on implementing each step of the above algorithm.

Algorithm 1.

0) Choose an index set $\mathbf{M} \in \mathbf{M}_{\text{all}}$ and a density contrast ρ_0 according to a priori information.
1) Initialize the level-set function ϕ according to the index set $\mathbf{M}$ obtained in step 0.
2) Compute the mismatch $G_s(\mathbf{r})$ along the boundary Γ according to equation 13 for each $s \in \mathbf{M}$.
3) Compute the Fréchet derivative in equation 16.
4) Evolve the level-set function according to the gradient flow (equation 18).
5) Reinitialize the level-set function to maintain the signed distance property.
6) Repeat steps 2–5 until it converges.

Step 0: The index set $\mathbf{M}$ *and the density contrast* ρ_0

In practice, any data type with the index set $\mathbf{M}$ being a subset of $\mathbf{M}_{\text{all}}$ can be used in an inversion because all five independent components $\{u_s\}_{s\in\mathbf{M}_{\text{all}}}$ can be measured by common gradiometers, such as the FTG system and the Falcon system; the FTG instrument measures all five independent components directly, and the Falcon instrument measures only u_{xy} and u_Δ, from which the other three components u_{xz}, u_{yz}, and u_{zz} are derived to minimize the high noise levels from vertical accelerations (Lee, 2001; Pilkington, 2012). For example, Li (2001b) develops an inversion method for all five independent components whereas Li (2010) uses only u_{xy} and u_Δ. However, many works have shown that not all of the five independent components are needed in illuminating source bodies.

Condi and Talwani (1999) find that u_{xy} and u_Δ can produce as accurate results as all of the five components together do. Zhdanov et al. (2004) suggest that using u_{xy} and u_Δ together can produce better results than u_{zz} alone whereas Fullagar and Pears (2010) suggest that using u_{zz} alone is the best choice and that inversion of multiple components adds little when u_{zz} is available. Martinez et al. (2010, 2013) compare u_{zz}, a combination of u_{xz}, u_{yz}, and u_{zz}, and a full-tensor-element combination, and show that u_{zz} is sufficient to produce geologically reasonable and interpretable results and that including additional components increases resolution. Pilkington (2012) investigates the information content provided by each of the tensor components and combinations thereof by using ideas from optimal survey design, and concludes that at smaller measurement-source distances, u_{zz} shows the best performance, whereas at larger measurement-source distances u_{xy}, u_Δ, and u_{xy}, combined with u_Δ, are the best performers. Because most publications suggest the use of components from u_{zz}, u_{xy}, and u_Δ, we consider mainly three cases in the following numerical examples: (1) $\mathbf{M} = \{xy, \Delta\}$, (2) $\mathbf{M} = \{zz\}$, (3) $\mathbf{M} = \{xy, \Delta, zz\}$.

Although subsurface source bodies may have arbitrary density contrast distributions, usually a range of density contrasts of subsurface source bodies can be determined from a priori information; We suggest to assign ρ_0 any value from that range in which the level-set formulation requires that the density contrast of subsurface source bodies be of the same value. This is reasonable when the minimum and maximum of the range are not far away from each other. For example, if the range of subsurface density contrast distribution is from $0.8\ \text{g/cm}^3$ to $1\ \text{g/cm}^3$, any constant ρ_0 in this range leads to at most a 25% overestimate of volume of some source body or 20% underestimate of that, which is acceptable in practice.

Step 1: Initialization of level-set function

Because there exist infinitely many pairs $\{\rho_0, D\}$ of density models that can produce the same measurement data, it is impossible to determine ρ_0 and D simultaneously. However, we expect that there may exist some intrinsic property of the domain D that is independent of ρ_0, and we expect that this intrinsic property may be beneficial to initialize the level-set function in Algorithm 1.

Motivated by this, we illustrate the relation between ρ_0 and D by studying a simple example, the point-source model as shown in Figure 1a. Let the computational domain Ω be the cuboid $[0,1] \times [1,2]$ km $\times [-0.4, 0]$ km and the measurement surface Γ be $[0,1] \times [1,2] \times \{z = 0.1\ \text{km}\}$. Assume that the density contrast distribution is a point source of mass $1\text{E}/\gamma$ at $\mathbf{r}_s = (0.5, 1.5, -0.15)^T$ km; i.e., $\rho(\mathbf{r}) = 1\text{E}\times\delta(\mathbf{r}-\mathbf{r}_s)/\gamma$, where the unit $\text{E} = 10^{-9}\ \text{s}^{-2}$. We collect the differential curvature data g_{xy} and g_Δ and the vertical gradient data g_{zz} at $33 \times 17 = 561$ mesh points that are uniformly distributed on $\Gamma = [0,1] \times [1,2] \times \{z = 0.1 \text{ km}\}$ in x- and y-directions. Patterns of data $\{g_s\}_{s\in\{xy,\Delta,zz\}}$ are shown in Figure 1b–1d.

Next, we try to determine the unknown domain D from two groups of data set $\{g_{xy}, g_\Delta\}$ and $\{g_{zz}\}$ for different values of ρ_0 by the level-set method, and we try to find the desired property from resulting solutions.

In the implementation, we uniformly discretize the computational domain $\Omega = [0,1] \times [1,2] \times [-0.4, 0]$ km into $41 \times 41 \times 17 = 28{,}577$ mesh points with grid size 0.25 km in each direction. Suppose

$$\rho_0 = \frac{1\text{E}/\gamma}{(4/3\pi(R/\text{km})^3)}, \tag{19}$$

where we consider three different cases: $R = 0.13, 0.1$, and 0.08 km. We determine the unknown domain D for the three cases using Algorithm 1, in which we initialize the level-set function to be

$$\phi_0 = 0.1 - \|\mathbf{r} - \mathbf{C}\|, \tag{20}$$

a sphere centered at $\mathbf{C} = (0.5, 1.5, -0.2)$ km. In fact, by Newton's shell theorem, the unknown domain D is exactly the sphere

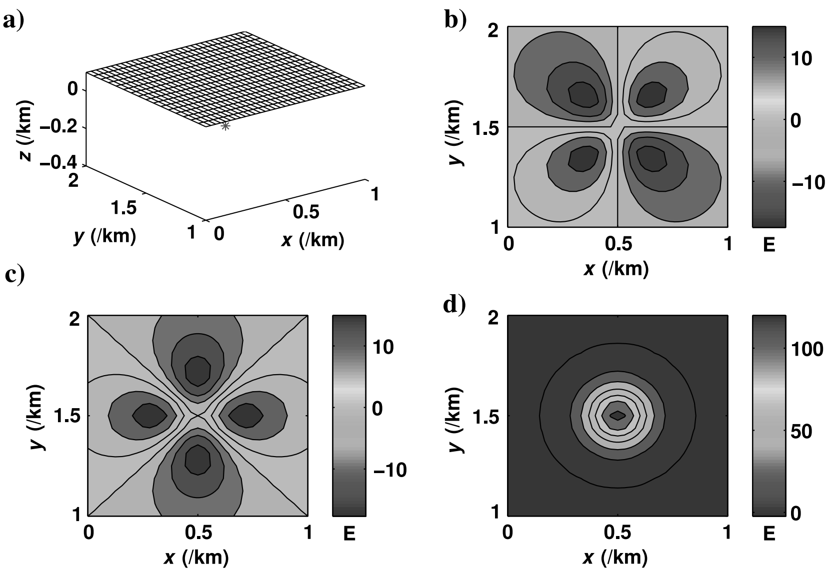

Figure 1. Point-source model: (a) source point $\mathbf{r}_s = [0.5, 1.5, -0.15]$ km marked by * underneath the measurement surface $\Gamma = [0,1] \times [1,2] \times \{z = 0.1 \text{ km}\}$, patterns of data: (b) g_{xy}, (c) g_Δ, and (d) g_{zz} on Γ (unit: $1\text{E} = 10^{-9}\ \text{s}^{-2}$).

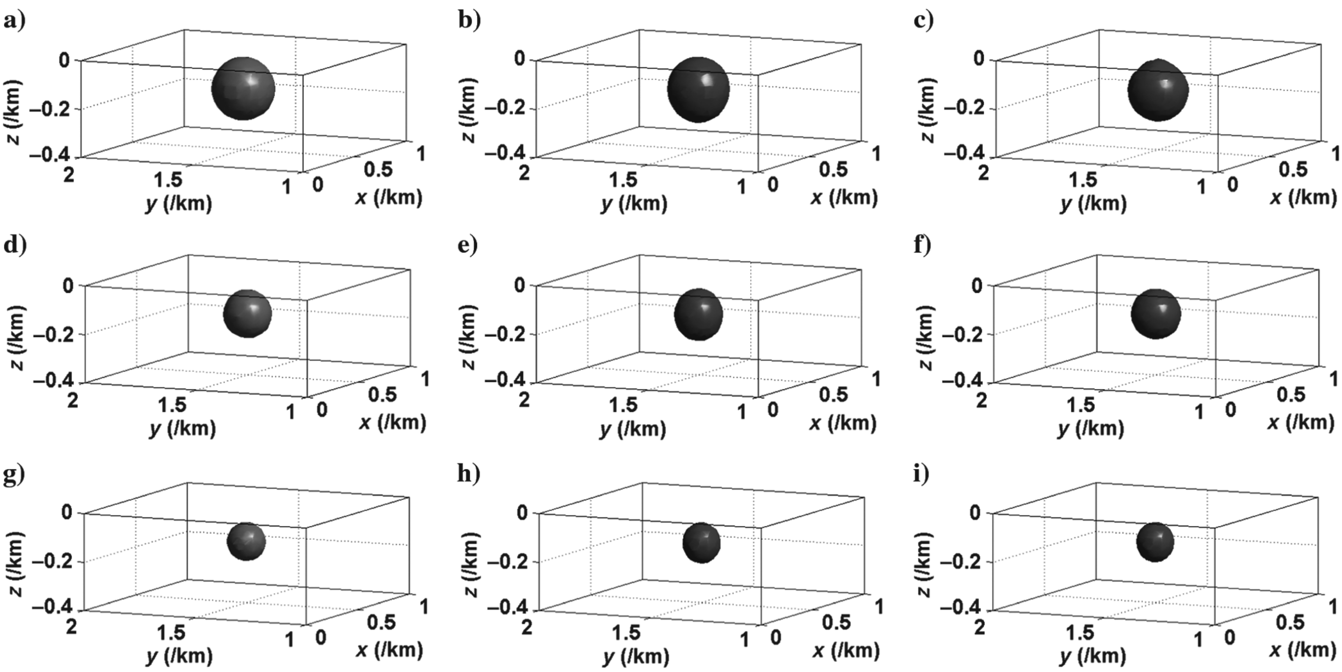

Figure 2. Point-source model: (a, d, and g) Shapes of exact solutions with $R = 0.13$ km in panel (a), $R = 0.1$ km in panel (d), and $R = 0.08$ km in panel (g). (b, e, and h) Shapes of numerical solutions for data g_{xy} and g_Δ, and (c, f, and i) for data g_{zz}. The density contrast $\rho_0 = 1\text{E}/\gamma/(4/3\pi(R/\text{km})^3)$ with $R = 0.13$ km in panels (b and c), $R = 0.1$ km in panels (e and f), and $R = 0.08$ km in panels (h and i).

centered at $\mathbf{r}_s$ with radius R when the density contrast $\rho_0 = 1\mathrm{E}/\gamma/(4/3\pi(R/\mathrm{km})^3)$, as plotted in Figure 2a, 2d, and 2g because this spherical source body and the point source have the same gravity center $\mathbf{r}_s$ and the same mass. For comparison, numerical solutions for inverting differential curvature data set $\{g_{xy}, g_\Delta\}$ for different values of R are plotted in Figure 2a, 2c, and 2e, whereas those for vertical gradient data $\{g_{zz}\}$ are plotted in Figure 2b, 2d, and 2f.

We make the following observations in Figure 2: Each numerical solution matches with the relevant exact solution very well for each case, and for either data set, the three numerical solutions with different density contrasts ρ_0 have the same gravity center $\mathbf{r}_s$ and seem to shrink to the gravity center $\mathbf{r}_s$ as ρ_0 increases. In other words, we numerically verify Newton's shell theorem by the local level-set method and find the following intrinsic property: Numerical solutions for different values of ρ_0 have the same gravity center. We believe that this property remains valid in general, and we may use this property to initialize the level-set algorithm. Specifically, if we can find the gravity center of each source body, then we consider a level-set function representing a few well-separated balls centered at those gravity centers to be a good initial level-set function because at least, this initial density model has the same gravity centers with the true model. Therefore, we are motivated to find the gravity centers to initialize the level-set algorithm.

Table 1. Running time for computing Fréchet derivatives, with the index set $\mathbf{M} = \{xy, \Delta\}$, in one iteration by two approaches in all numerical examples.

	Direct matrix-vector multiplication (s)	Low-rank-matrix decomposition algorithm (s)
Two cubes	0.95	0.05
Three cuboids	2.36	0.12
Two dikes	11.06	0.32
Five cuboids	9.53	0.38

To this end, we can use existing noniterative fast imaging methods, such as the depth from the extreme points method (Fedi, 2007), the migration method (Zhdanov et al., 2011), and so on. However, Cella and Fedi (2012) and Fedi and Pilkington (2012) find that a physically dependent depth-weighting function should be chosen in those depth-weighting-based imaging methods; otherwise, these methods may locate sources at incorrect depths. Nevertheless, our level-set-based inversion does not depend on depth-weighting functions so that it is still reasonable to use imaging methods with physically independent weighting functions for locating sources and gravity centers in terms of initializing the level-set algorithm. Thus, we apply the migration method (Zhdanov et al., 2011) to recover rough source locations. We will see from numerical results that an initial level-set function, with inaccurate depths or even inconsistent number of source bodies, can still be evolved to a reasonable solution matching with true models.

In some cases when subsurface source bodies are not well separated, the aforementioned fast imaging methods may lose effectiveness (Cella and Fedi, 2012; Fedi and Pilkington, 2012). In this situation, we choose to use the following iterative L^1-regularization method so that subsurface source bodies may be resolved more easily.

In the context of the inverse gradiometry problem, because the density contrast distribution ρ is assumed to have a compact support in Ω, we look for a density contrast distribution ρ with compact support in Ω so that extrema among the nonzeros may exhibit positions of the gravity centers. Because the L^1-norm-based regularization promotes compact support (Brezis, 1974; Ozolins et al., 2013), we propose to solve for the desired density distribution the following nonlinear optimization problem:

$$\min_\rho \tilde{F}(\rho) := \min_\rho \left\{ \sum_{s\in\mathbf{M}} \left\| 4\pi\gamma \int_\Omega K_s(\cdot,\tilde{\mathbf{r}})\rho(\tilde{\mathbf{r}})d\tilde{\mathbf{r}} - g_s(\cdot) \right\|^2_{L^2(\Gamma)} + \lambda \|W\rho\|_{L^1(\Omega)} \right\}, \tag{21}$$

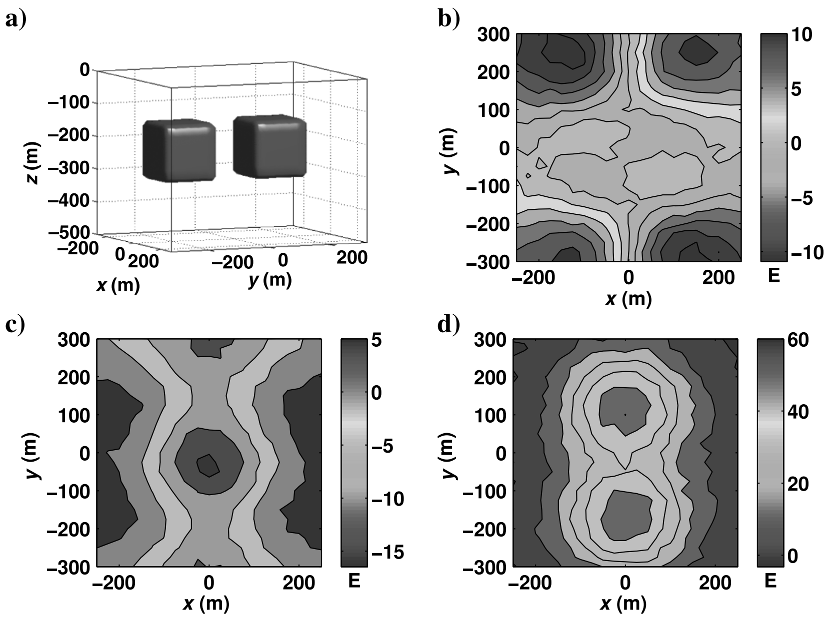

Figure 3. Two cubes: (a) true positions of the source bodies. Observed data: (b) g_{xy}, (c) g_Δ, and (d) g_{zz} on the ground surface $\Gamma = [-250, 250] \times [-300, 300] \times \{z = 0 \text{ m}\}$ polluted with 3% Gaussian noise (unit: E).

where $\lambda > 0$ is the penalty parameter. Here, the depth-weighting function W is chosen according to Li and Oldenburg (1998) and Li (2001b) as

$$W(\tilde{\mathbf{r}}) = d(\tilde{\mathbf{r}}, \Gamma)^{-\beta/2} \tag{22}$$

for $\beta = 2$ with $d(\tilde{\mathbf{r}}, \Gamma)$ being the depth of $\tilde{\mathbf{r}}$ below the planar surface Γ.

Assuming that Ω is discretized by N points and that there are M observation points on Γ, we apply trapezoidal quadrature rules to discretize the relevant integrals in the above optimization problem, and we end up with the following finite-dimensional optimization problem in matrix form:

$$\min_{\boldsymbol{\rho}} \tilde{F}(\boldsymbol{\rho}) := \min_{\boldsymbol{\rho}} \{||\mathbf{K}\boldsymbol{\rho} - \mathbf{b}||_2^2 + \lambda||\mathbf{W}\boldsymbol{\rho}||_1\}, \tag{23}$$

where $\boldsymbol{\rho} \in \mathbb{R}^{N\times 1}$ represents the unknown density ρ at the N mesh points in Ω, $\mathbf{b} \in \mathbb{R}^{M\times 1}$ represents measurement data g_s at the M observation points for all $s \in \mathbf{M}$, matrix $\mathbf{K} \in \mathbb{R}^{M\times N}$ and the diagonal matrix $\mathbf{W} \in \mathbb{R}^{N\times N}$ are related to the kernel and weighting functions K_s and W, respectively, and $\|\cdot\|_l$ represents the l-norm for $l = 1, 2$. We apply the l1_ls package (Koh et al., 2007) to solve this nonlinear minimization problem (equation 23). In our implementation, the L^1-regularization solution of problem 23 is computed on very coarse meshes because rough locations of gravity centers are adequate for our level-set algorithm.

Steps 2 and 3: Computing the mismatch functional and the Fréchet derivative

To compute the mismatch functional, one may adopt the wavelet compression (Li and Oldenburg, 2003) and the finite-difference forward solver (Farquharson and Mosher, 2009). Because the kernel matrix $K_s(\mathbf{r}, \tilde{\mathbf{r}})$ in equation 4 decays rapidly as the distance $|\mathbf{r} - \tilde{\mathbf{r}}|$

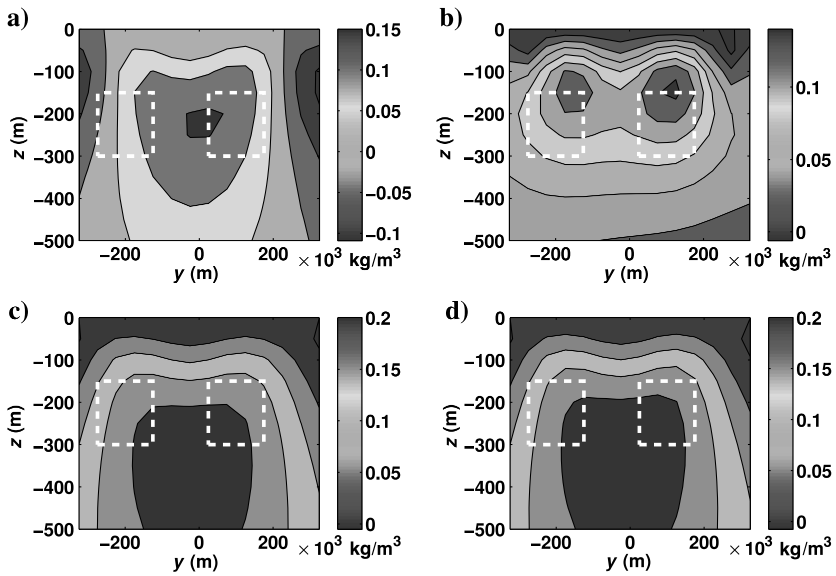

Figure 4. Two cubes: Cross sections of migration density at $x = 0$ m by migrating single-index data: (a) g_{xy}, (b) g_Δ, (c) g_{zz}, and combined data (d) g_{xy}, g_Δ, and g_{zz}.

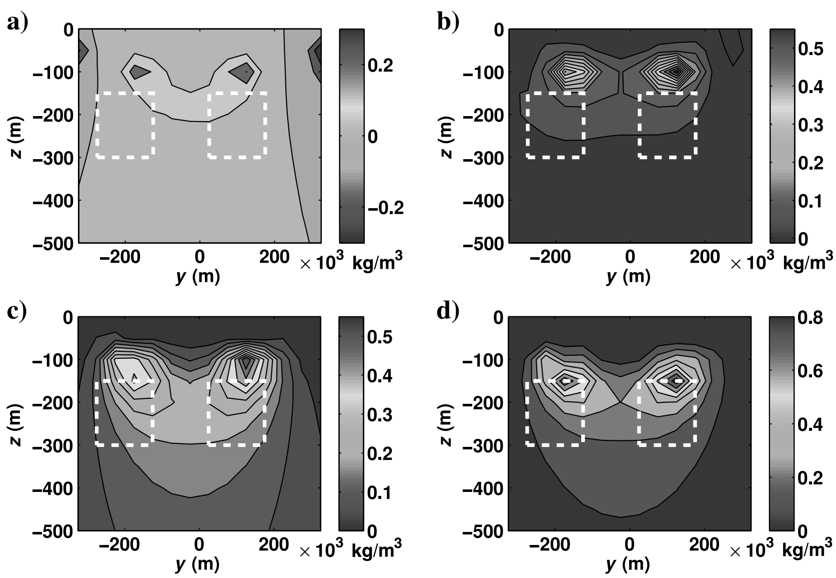

Figure 5. Two cubes: Cross sections of L^1-regularization solutions at $x = 0$ m for single-index data: (a) g_{xy}, (b) g_Δ, (c) g_{zz}, and combined data (d) g_{xy}, g_Δ, and g_{zz}. Dashed lines indicate the true positions of source bodies.

increases, the low-rank-matrix decomposition algorithm proposed by W. Lu (personal communication, 2014) can be used to speed up matrix-vector multiplications arising in computing the mismatch and the Fréchet derivative. To avoid numerical instabilities (Zhao et al., 1996), the delta function $\delta(\phi)$ in equation 17 is approximated by $\delta_\epsilon(\phi) = \chi_{T_\epsilon}|\nabla\phi|$, with support $T_\epsilon = \{\mathbf{p} \in \Omega : |\phi(\mathbf{p})| \leq \epsilon\} \subset\subset \Omega$ for some $\epsilon > 0$.

To illustrate the performance of this low-rank-matrix decomposition algorithm, as listed in Table 1, we record running times for computing the Fréchet derivative, with the index set $\mathbf{M} = \{xy, \Delta\}$, in one iteration by two different approaches, direct computation and the low-rank-matrix decomposition algorithm, for the numerical examples studied in this work with the same setups. We can clearly see that the improvement is dramatic.

Steps 4 and 5: Computing gradient descent flows

Standard techniques apply; see, Isakov et al. (2011) for details. Related techniques have been widely used in the level-set community in various applications (Osher and Sethian, 1988; Qian and

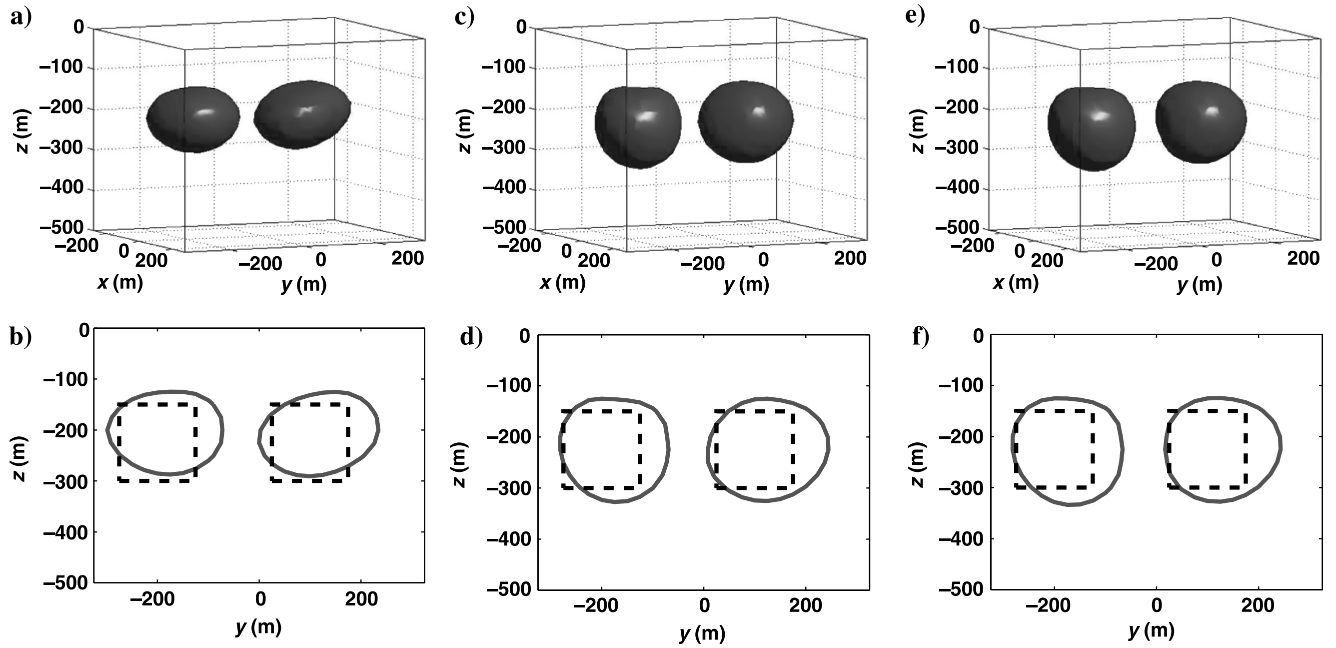

Figure 6. Two cubes with $\rho_0 = 1 \times 10^3$ kg/m^3. Shapes of numerical solutions at the 6000th iteration with a two-sphere initial guess for the index set (a) $\mathbf{M} = \{xy, \Delta\}$, (c) $\mathbf{M} = \{zz\}$, and (e) $\mathbf{M} = \{xy, \Delta, zz\}$. (a, c, and e) Cross sections of solutions at $x = 0$ m are plotted with solid lines in panels (b, d, and f), respectively. Dashed rectangles indicate the true positions of source bodies.

Figure 7. Two cubes with $\rho_0 = 1 \times 10^3$ kg/m^3 and the index set $\mathbf{M} = \{xy, \Delta\}$. Shapes of the level-set function at the (a) 0th (the initial guess being a sphere of radius 50 m centered at $[0, -200, -150]$ m), (b) 2000th, (c) 4000th, and (d) 6000th iterations.

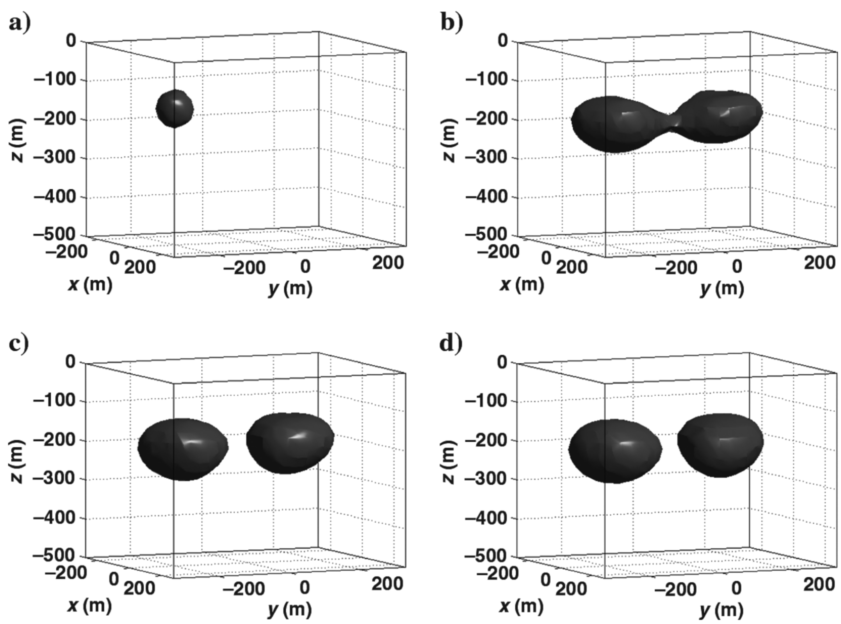

Symes, 2002a, 2002b; Qian et al., 2003; Leung et al., 2004; 2007; Qian and Leung, 2004, 2006; Cecil et al., 2006). To avoid numerical instabilities as addressed by Isakov et al. (2011), the Heaviside function is approximated by the ϵ-Heaviside function as

$$H_\epsilon(\phi)=\begin{cases}0, & \phi<-\epsilon,\\ \frac{1}{2}+\frac{\phi}{2\epsilon}+\frac{1}{2\pi}\sin\left(\frac{\pi\phi}{\epsilon}\right), & -\epsilon\le\phi\le\epsilon,\\ 1, & \phi>\epsilon.\end{cases} \tag{24}$$

NUMERICAL RESULTS

We study several synthetic examples in terms of three different index sets: $\mathbf{M}=\{xy,\Delta\}$, $\mathbf{M}=\{zz\}$, and $\mathbf{M}=\{xy,\Delta,zz\}$.

Two cubes

We first study a two-cube model as shown in Figure 3a, which was previously studied by Zhdanov et al. (2004). The target domain D consists of two identical cubes; they have sides of length 150 m,

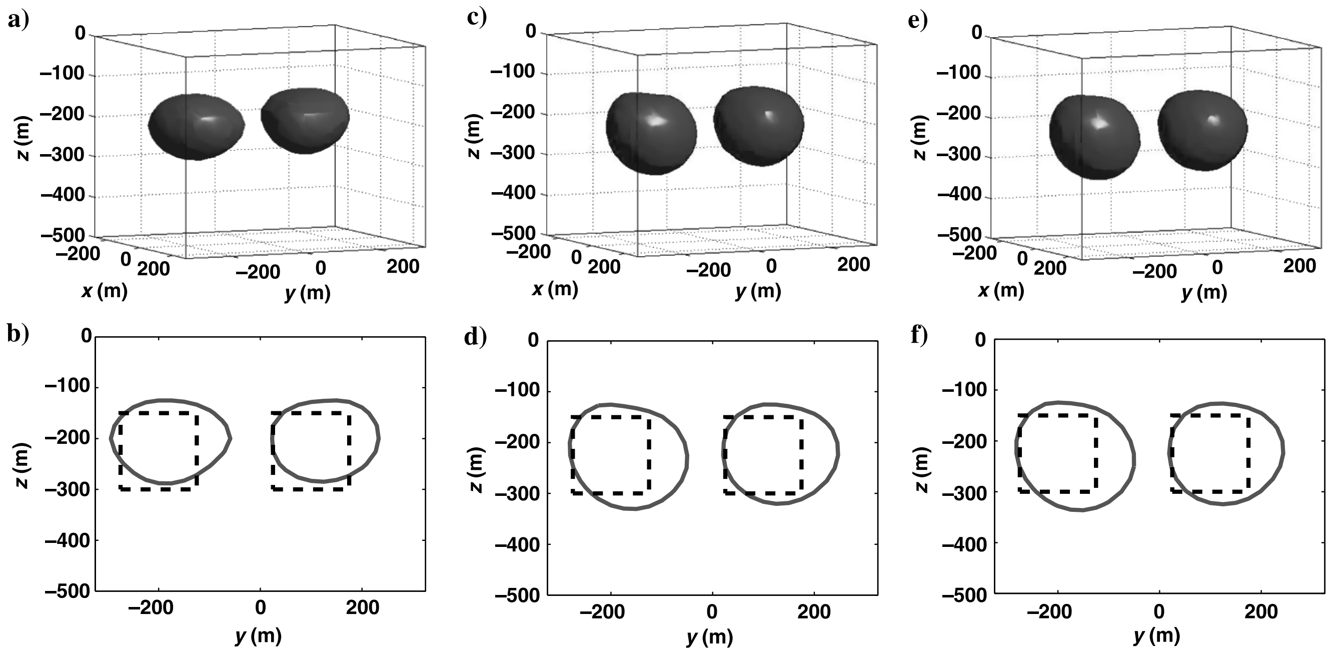

Figure 8. Two cubes with $\rho_0 = 1\times10^3$ kg/m^3. Shapes of numerical solutions with a one-sphere initial guess at the 6000th iteration for (a) $\mathbf{M}=\{xy,\Delta\}$, (c) $\mathbf{M}=\{zz\}$, and (e) $\mathbf{M}=\{xy,\Delta,zz\}$. Cross sections of solutions in panels (a, c, and e) at $x=0$ m are plotted with solid lines in panels (b, d, and f), respectively. Dashed rectangles indicate the true positions of source bodies.

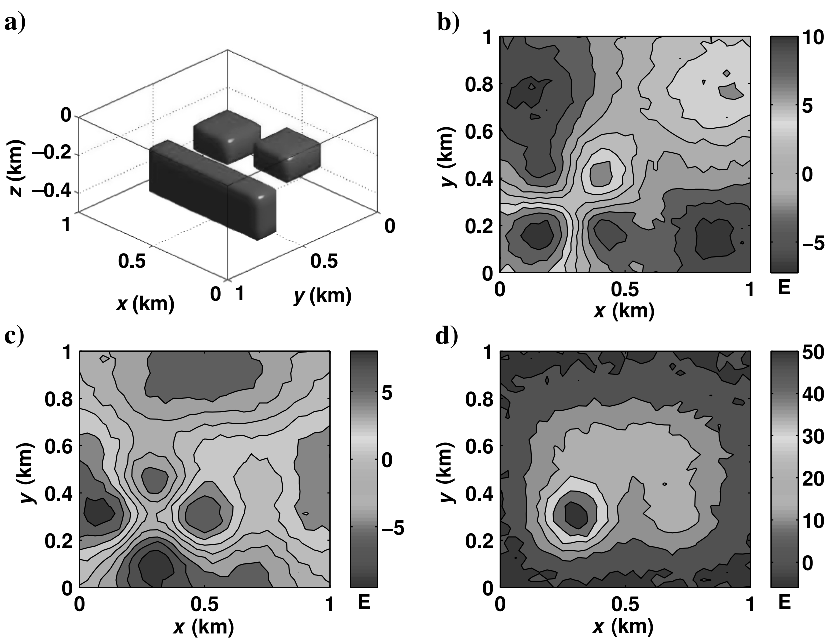

Figure 9. Three cuboids: (a) true positions of the source bodies with $\rho_0 = 1\times10^3$ kg/m^3. Observed data polluted with 3% Gaussian noise (unit: E) in panel (b) g_{xy}, (c) g_Δ, and (d) g_{zz} on the ground surface $\Gamma = [0,1] \times [0,1] \times \{z=0 \text{ km}\}$.

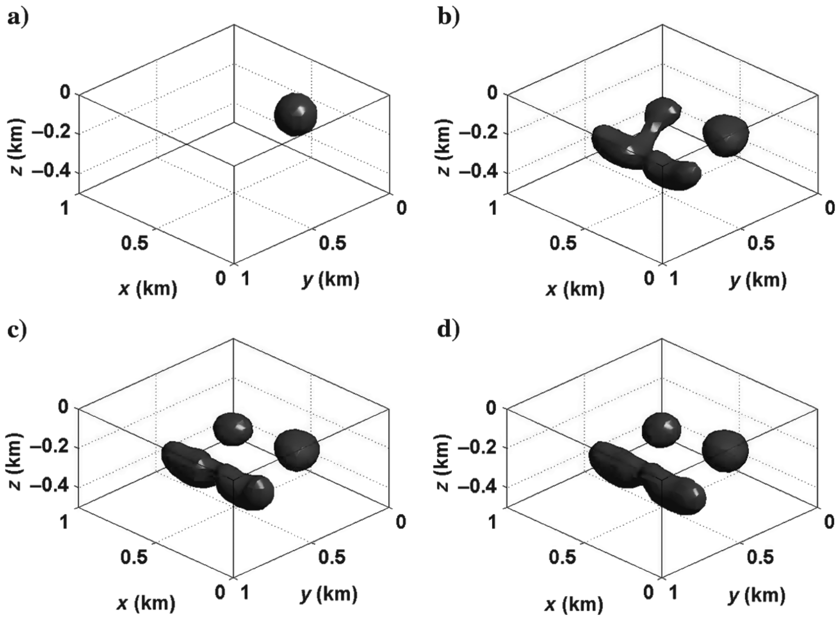

Figure 10. Three cuboids with $\rho_0 = 1 \times 10^3\ \mathrm{kg/m^3}$ and $\mathbf{M} = \{xy, \Delta\}$. Shapes of the level-set function at the (a) 0th (the initial guess being a sphere of radius 0.09 km centered at $[0.3, 0.3, -0.1]$ km), (b) 2000th, (c) 4000th, and (d) 6000th iterations.

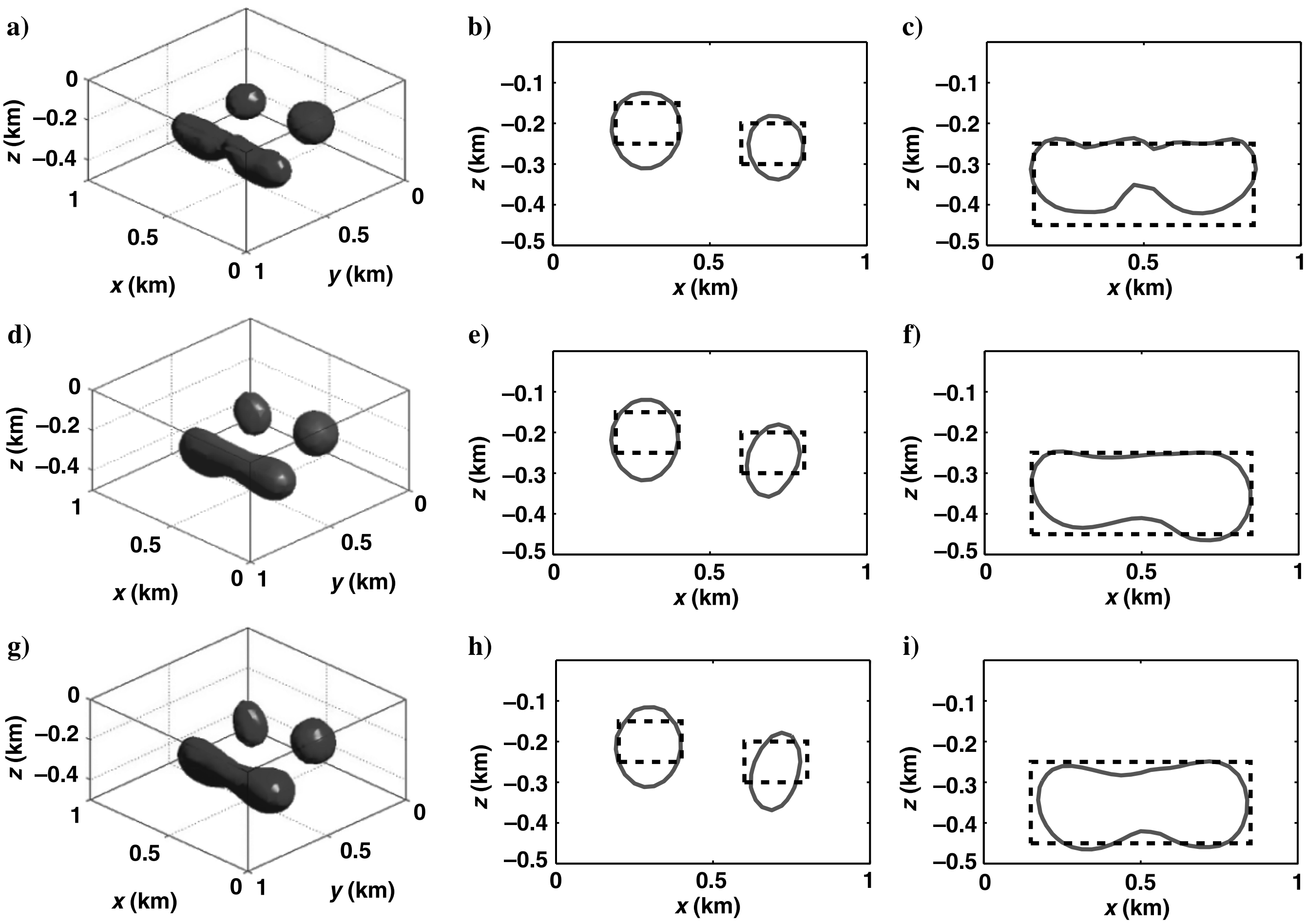

Figure 11. Three cuboids with $\rho_0 = 1 \times 10^3\ \mathrm{kg/m^3}$. Shapes of numerical solutions at the 6000th iteration for (a) $\mathbf{M} = \{xy, \Delta, zz\}$, (d) $\mathbf{M} = \{zz\}$, and (g) $\mathbf{M} = \{xy, \Delta, zz\}$. Cross sections of solutions in panels (a, d, and g) at $y = 10/32$ km plotted with solid lines in panels (b, e, and h), respectively. Cross sections of solutions in panels (a, d, and g) at $y = 19/32$ km plotted with solid lines in panels (c, f, and i), respectively. Dashed rectangles indicate the true positions of the source bodies.

are 150 m under the surface, and are 150 m apart; the density contrast in both cubes over the background is 1×10^3 kg/m^3.

To be consistent with Zhdanov et al. (2004), we take the subsurface domain $\Omega = [-275,275] \times [-325,325] \times [-500,0]$ m and assume that there are $21 \times 25 = 525$ observation points on the ground surface $\Gamma = [-250,250] \times [-300,300] \times \{z = 0\,\mathrm{m}\}$, which are uniformly distributed with grid size 25 m in the x- and y-directions. To collect data g_{xy}, g_{Δ}, and g_{zz}, we compute u_{xy}, u_{Δ}, and u_{zz} by equation 8, and we use the trapezoidal rule to approximate the volume integral over the domain D, which is assumed to be uniformly discretized with grid size 25 m in all three directions. We further add 3% Gaussian noise to the resulting u_{xy}, u_{Δ}, and u_{zz}, and we obtain the data set $\{g_{xy}, g_{\Delta}, g_{zz}\}$ as shown in Figure 3b–3d.

To initialize the level-set algorithm, we use the migration method and the weighted L^1-regularization method to locate gravity centers of source bodies. In the implementation, we uniformly discretize Ω into $12 \times 14 \times 11$ mesh points with grid size 50 m in all directions. We migrate four different data sets: $\{g_{xy}\}$, $\{g_{\Delta}\}$, $\{g_{zz}\}$, and $\{g_{xy}, g_{\Delta}, g_{zz}\}$ to find corresponding migration densities; meanwhile, we compute the weighted L^1-regularized solution for the same four data sets by solving problem 23. From the eight numerical solutions, we capture extrema at $x = 0$ m for both methods, as shown in Figures 4 and 5, in which dashed lines show the true positions of the source bodies.

Among the four migration densities shown in Figure 4, the migration density ρ_{Δ}^* in Figure 4b resolves the two source bodies. In contrast, all four L^1-regularization solutions in Figure 5 resolve the two source bodies. From extrema shown in Figures 4b and 5, we initialize the level-set function to be two well-separated spheres of the same radius 50 m, centered at $(0, -200, -150)$ m and $(0, 50, -150)$ m, respectively.

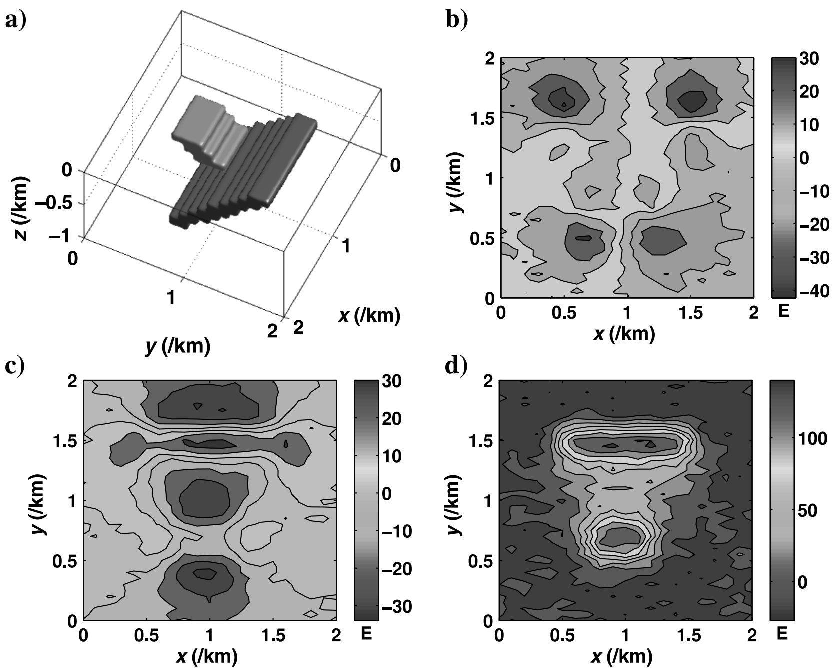

Figure 12. Two dikes: (a) true positions of the source bodies, where $\rho_0 = 0.8$ g/cm^3 in the short dike whereas $\rho_0 = 1.0$ g/cm^3 in the long dike. Observed data (b) g_{xy}, (c) g_{Δ}, and (d) g_{zz} on the ground surface $\Gamma = [0,2] \times [0,2] \times \{z = 0$ km$\}$; all are polluted by 5% Gaussian noise.

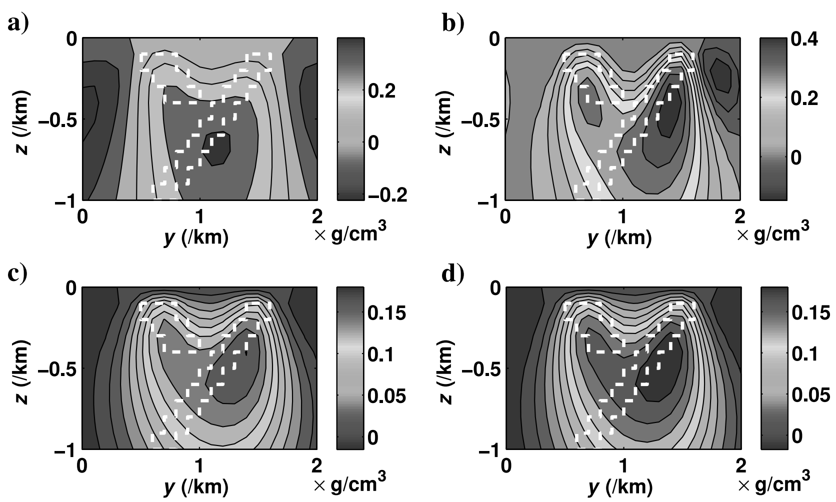

Figure 13. Two dikes: (a) Cross sections of the migration density at $x = 1$ km by migrating single-index data g_{xy}, (b) g_{Δ}, and (c) g_{zz}, and (d) combined data g_{xy}, g_{Δ}, and g_{zz}.

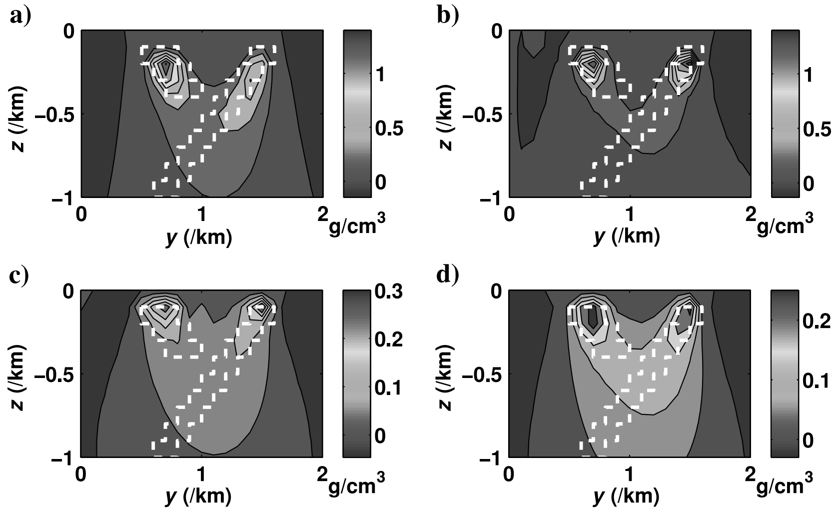

Figure 14. Two dikes: (a) Cross sections of L^1-regularized solutions at $x = 1$ km for single-index data g_{xy}, (b) g_Δ, (c) g_{zz}, and (d) combined data g_{xy}, g_Δ, and g_{zz}. The dashed lines indicate the true positions of the source bodies.

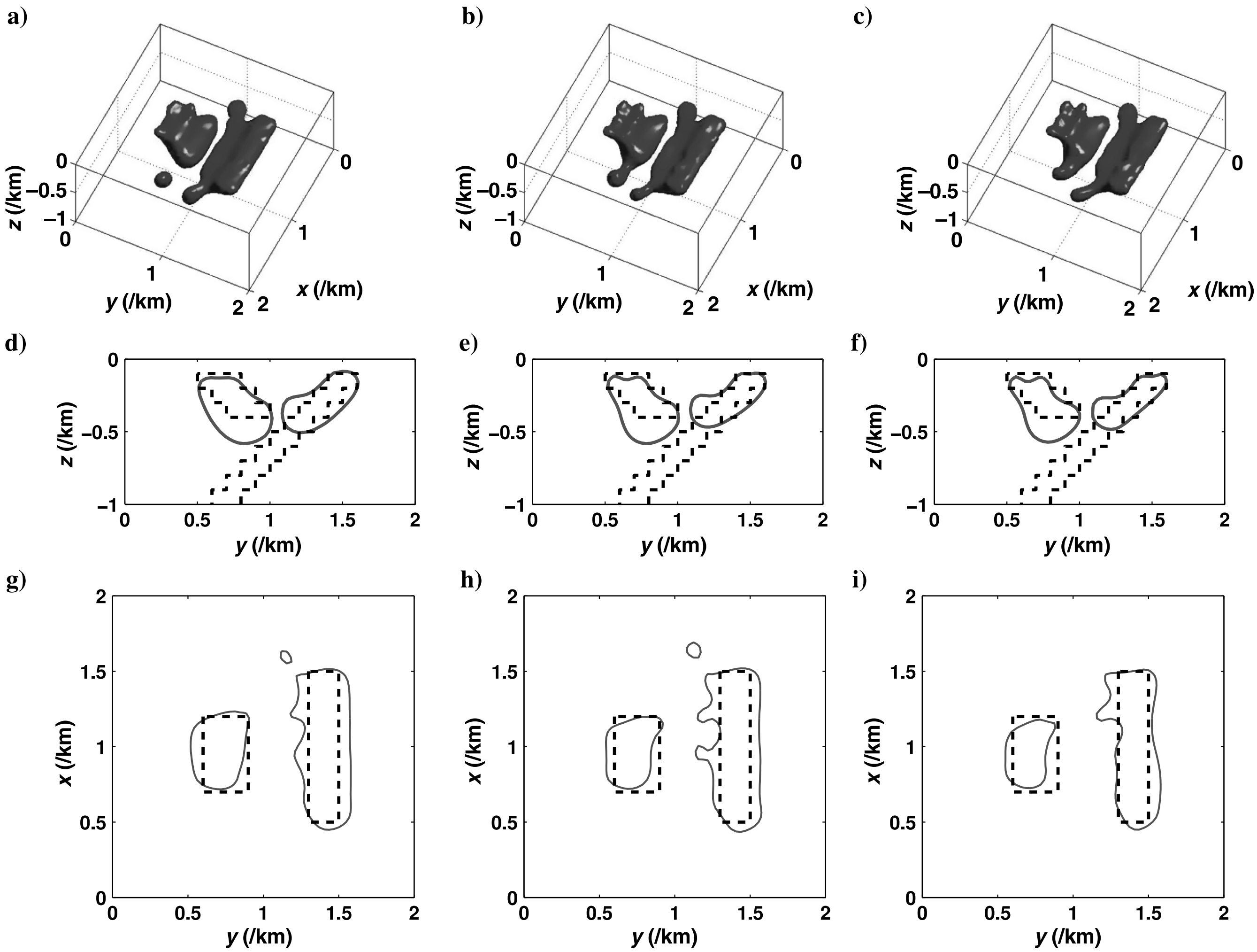

Figure 15. Two dikes: Shapes of numerical solutions at the 2000th iteration with the index set $\mathbf{M} = \{xy, \Delta\}$ and a two-sphere initial guess; (a) $\rho_0 = 0.8$ g/cm^3, (b) $\rho_0 = 0.9$ g/cm^3, (c) $\rho_0 = 1.0$ g/cm^3, (d-f) cross sections of the numerical solutions in (a-c) at $x = 1$ km, and (g-i) cross sections of the numerical solutions in (a-c) at $z = -0.25$ km. The dashed lines indicate the true positions of the target.

To apply the level-set algorithm, we take ρ_0 to be the exact value, i.e., $\rho_0 = 1 \times 10^3\ \mathrm{kg/m^3}$, and rediscretize the computational domain Ω into $23 \times 27 \times 21$ uniform mesh points with the same grid size 25 m in all directions.

For all three index sets: $\mathbf{M} = \{xy, \Delta\}$, $\mathbf{M} = \{zz\}$, and $\mathbf{M} = \{xy, \Delta, zz\}$, we compute related numerical solutions based on the above setup. To compare the performance of the three index sets in Figure 6, we plot shapes of the three numerical solutions at the 6000th iteration and cross sections of those solutions at $x = 0$ m, in which the dashed lines show the true positions of the source bodies. We can see that for all three index sets, the level-set algorithm produces numerical solutions that match with true source bodies reasonably well and locate source bodies at true depths.

To test robustness of the level-set algorithm, we initialize the level-set function to be a single sphere of radius 50 m centered at $(0, -200, -150)$ m and then compute numerical solutions for all three index sets: $\mathbf{M} = \{xy, \Delta\}$, $\mathbf{M} = \{zz\}$, and $\mathbf{M} = \{xy, \Delta, zz\}$.

For $\mathbf{M} = \{xy, \Delta\}$, we plot numerical solutions at different iterations as shown in Figure 7. We can see that the level-set algorithm succeeds in splitting the single source body into two and numerical solutions become steady after 4000 iterations. For the other two index sets $\mathbf{M} = \{zz\}$ and $\mathbf{M} = \{xy, \Delta, zz\}$, we compute numerical solutions by using the same initial level-set function. In comparison with the true model, we show, for all three index sets, numerical solutions and their cross sections at $x = 0$ m at the 6000th iteration in Figure 8. We can see that for all three index sets, the level-set algorithm even with an unreasonable initial guess still produces numerical solutions that match with true source bodies reasonably well and locate source bodies at true depths.

Three cuboids

We next study a model with three source bodies, consisting of two short cuboids and one long cuboid, as shown in Figure 9a. The density contrast in all source bodies is $1 \times 10^3\ \mathrm{kg/m^3}$. We take the computational domain $\Omega = [0, 1] \times [0, 1] \times [-0.5, 0]$ km and as-

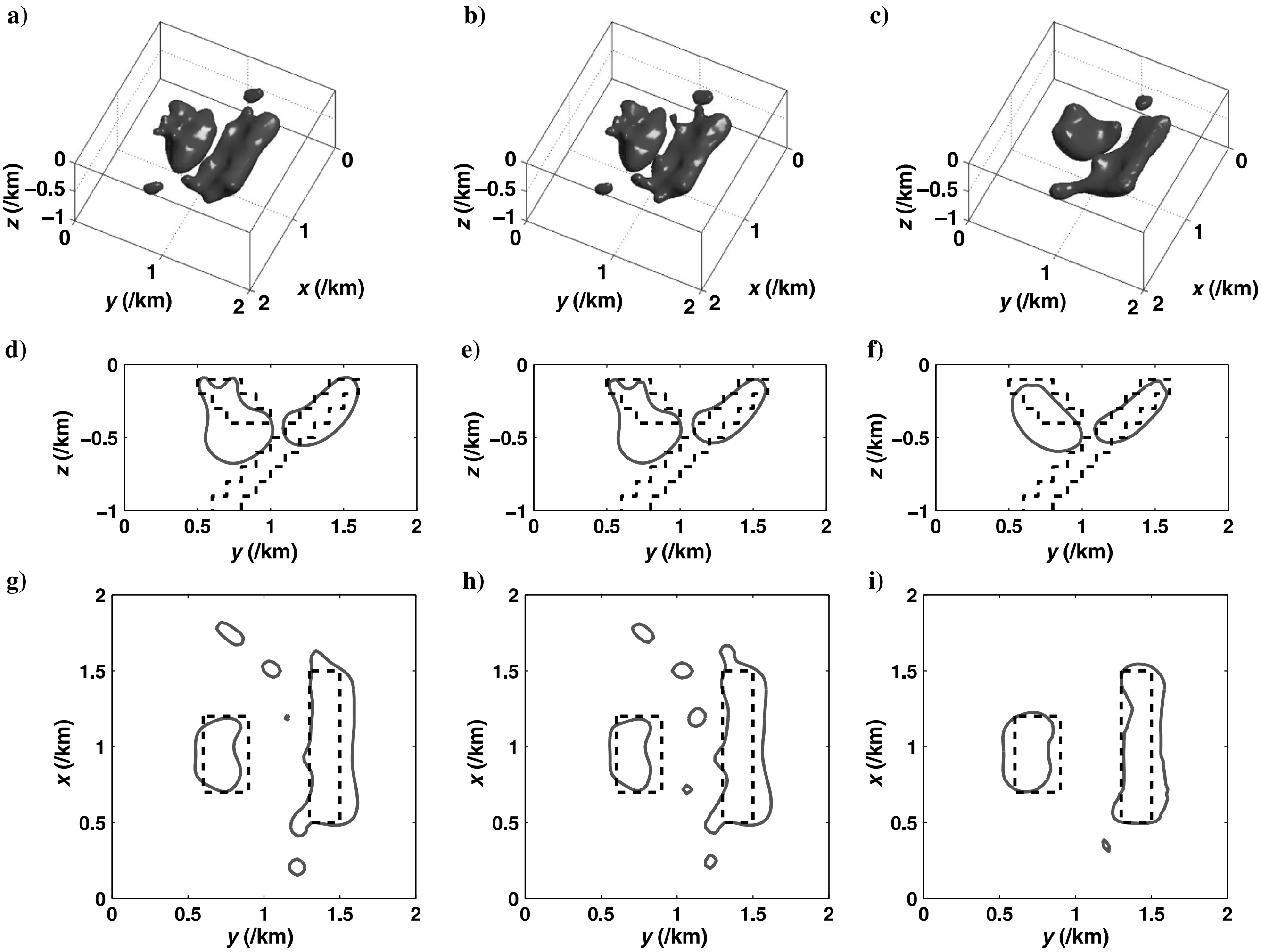

Figure 16. Two dikes: Shapes of numerical solutions at the 2000th iteration with the index set $\mathbf{M} = \{zz\}$ and a two-sphere initial guess; (a) $\rho_0 = 0.8\ \mathrm{g/cm^3}$, (b) $\rho_0 = 0.9\ \mathrm{g/cm^3}$, (c) $\rho_0 = 1.0\ \mathrm{g/cm^3}$, (d-f) cross sections of the numerical solutions in (a-c) at $x = 1$ km, and (g-i) cross sections of the numerical solutions in (a-c) at $z = -0.25$ km. The dashed lines indicate the true positions of the target.

sume that there are $33 \times 33 = 1089$ observation points, uniformly distributed on the surface $\Gamma = [0,1] \times [0,1] \times \{z = 0 \text{ km}\}$ with grid size $1/32$ km in the x- and y-directions. To collect data g_{xy}, g_Δ, and g_{zz}, we compute u_s by equation 23 for $s = xy, \Delta, zz$ and use the trapezoidal rule to approximate the volume integral over the domain D, which is uniformly discretized with grid size $1/32$ km in all three directions. We further add 3% Gaussian noise to the resulting u_{xy}, u_Δ, and u_{zz} and obtain the data set $\{g_{xy}, g_\Delta, g_{zz}\}$ as shown in Figure 9b–9d.

To initialize the level-set algorithm, we use the migration method and the weighted L^1-regularization method to locate gravity centers of source bodies. In the implementation, we uniformly discretize the computational domain Ω into $21 \times 21 \times 11$ mesh points with grid size 0.05 km in all directions. We migrate four different data sets: $\{g_{xy}\}$, $\{g_\Delta\}$, $\{g_{zz}\}$, and $\{g_{xy}, g_\Delta, g_{zz}\}$ to find corresponding migration densities; meanwhile, we compute the weighted L^1-regularized solution for the same four data sets by solving problem 23. From the eight numerical solutions, we capture only one extremum around the point $(0.3, 0.3, -0.1)$ km, and therefore, we initialize the level-set function to be a single sphere of radius 0.09 km centered at $(0.3, 0.3, -0.1)$ km, as shown in Figure 10a.

To apply the level-set algorithm, we take ρ_0 to be the exact value, i.e., $\rho_0 = 1 \times 10^3$ kg/m^3, and we rediscretize the computational domain Ω into $33 \times 33 \times 17$ uniform mesh points with the same grid size $1/32$ km in all directions.

For $\mathbf{M} = \{xy, \Delta\}$, by the level-set algorithm, we obtain numerical solutions at different iterations as shown in Figure 10. We can see that the level-set algorithm succeeds in resolving all source bodies completely after 4000 iterations, and numerical solutions converge to a steady state.

For the other two index sets $\mathbf{M} = \{zz\}$ and $\mathbf{M} = \{xy, \Delta, zz\}$, we compute related numerical solutions with the same setup. To compare the performance of the three index sets, in Figure 11, we plot shapes of the three numerical solutions at the 6000th iteration and cross sections of those solutions at $y = 10/32$ and $19/32$ km, in which the dashed lines show true positions of source bodies. We can

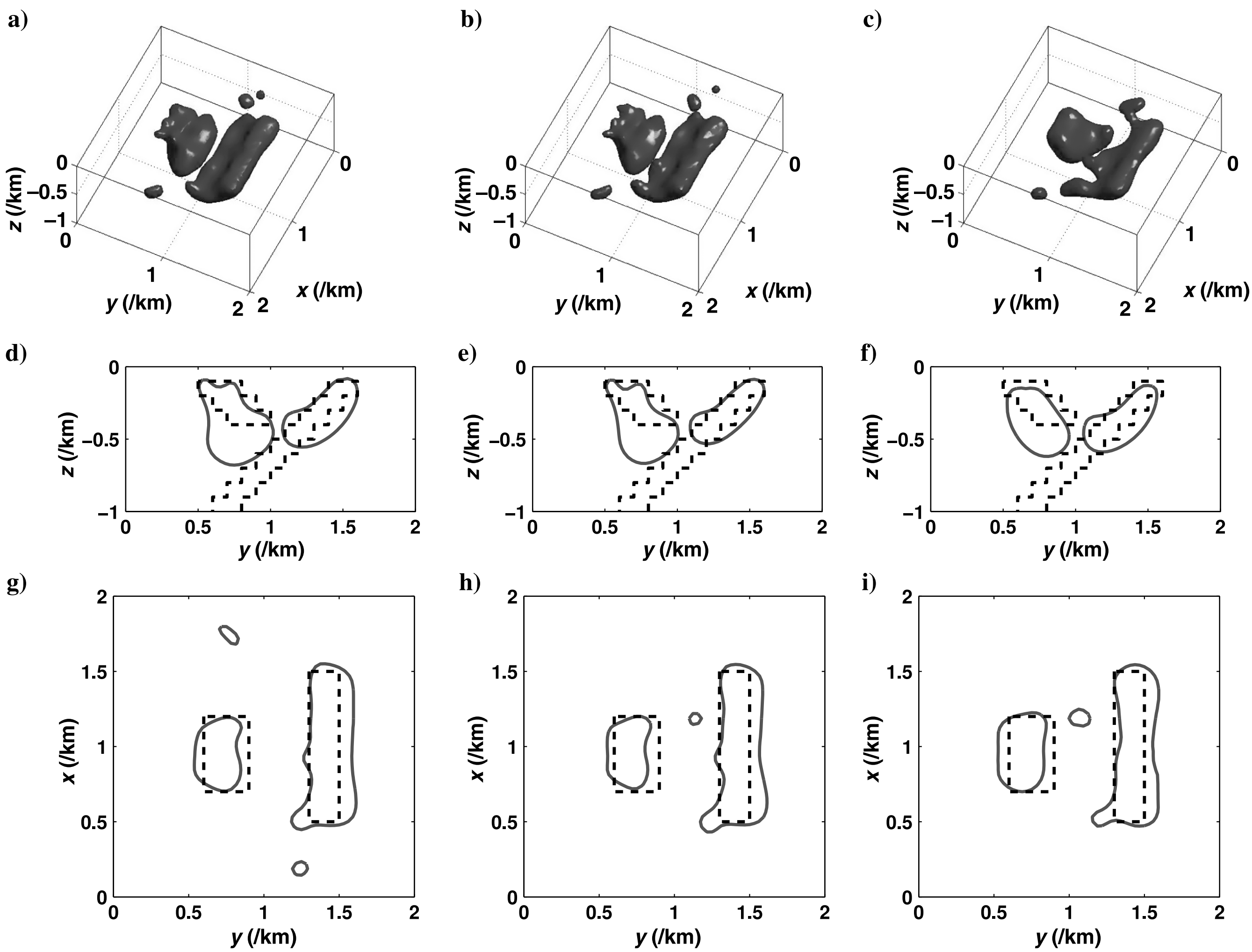

Figure 17. Two dikes: Shapes of numerical solutions at the 2000th iteration with the index set $\mathbf{M} = \{xy, \Delta, zz\}$ and a two-sphere initial guess; (a) $\rho_0 = 0.8$ g/cm^3, (b) $\rho_0 = 0.9$ g/cm^3, (c) $\rho_0 = 1.0$ g/cm^3, (d-f) cross sections of the numerical solutions in (a-c) at $x = 1$ km, and (g-i) cross sections of the numerical solutions in (a-c) at $z = -0.25$ km. The dashed lines indicate the true positions of the target.

see that for all three index sets, the level-set algorithm produces numerical solutions that match with the true source bodies reasonably well and locate the source bodies at true depths.

Two dikes

We next study a more complicated model as shown in Figure 12a, where the target domain D consists of two well-separated dikes, and the density contrast of the short dike is $0.8\ \mathrm{g/cm^3}$ whereas that of the long dike is $1\ \mathrm{g/cm^3}$. This example was previously studied in the inversion of gravimetry data by Li and Oldenburg (1998), and we use this example to check applicability of the level-set algorithm to source bodies with different density contrasts.

To be consistent with Li and Oldenburg (1998), we take the subsurface domain $\Omega = [0,2] \times [0,2] \times [-1,0]$ km and assume that there are $21 \times 41 = 861$ observation points on the surface $\Gamma = [0,2] \times [0,2] \times \{z = 0\ \mathrm{km}\}$, which are uniformly distributed with grid sizes of 0.1 and 0.05 km in the x- and y-directions, respectively. To collect the data set $\{g_{xy}, g_\Delta, g_{zz}\}$, we compute u_{xy}, u_Δ, and u_{zz} by equation 8 and use the trapezoidal rule to discretize the volume integral over the domain D, which is uniformly discretized with grid size $1/32$ km in all directions. We then add 5% Gaussian noise to the resulting u_{xy}, u_Δ, and u_{zz}, and we obtain the data set $\{g_{xy}, g_\Delta, g_{zz}\}$ as shown in Figure 12b–12d.

To initialize the level-set algorithm, we use the migration method and the weighted L^1-regularization method to locate gravity centers of source bodies. In the implementation, we uniformly discretize the computational domain Ω into $21 \times 21 \times 11$ mesh points with a grid size of 0.1 km in all directions. We migrate four different data sets: $\{g_{xy}\}$, $\{g_\Delta\}$, $\{g_{zz}\}$, and $\{g_{xy}, g_\Delta, g_{zz}\}$ to find corresponding migration densities; meanwhile, we compute the weighted L^1-regularized solution for the same four different data sets by solving problem 23. From the eight numerical solutions, we capture extrema at $x = 1$ km for both methods, as shown in Figures 13 and 14, in which the dashed lines show the true positions of the source bodies.

Among the four migration densities shown in Figure 13, the migration density ρ^*_Δ in Figure 13b resolves the two source bodies. In contrast, all four L^1-regularization solutions in Figure 14 resolve the two source bodies. From the extrema shown in Figures 13b and 14,

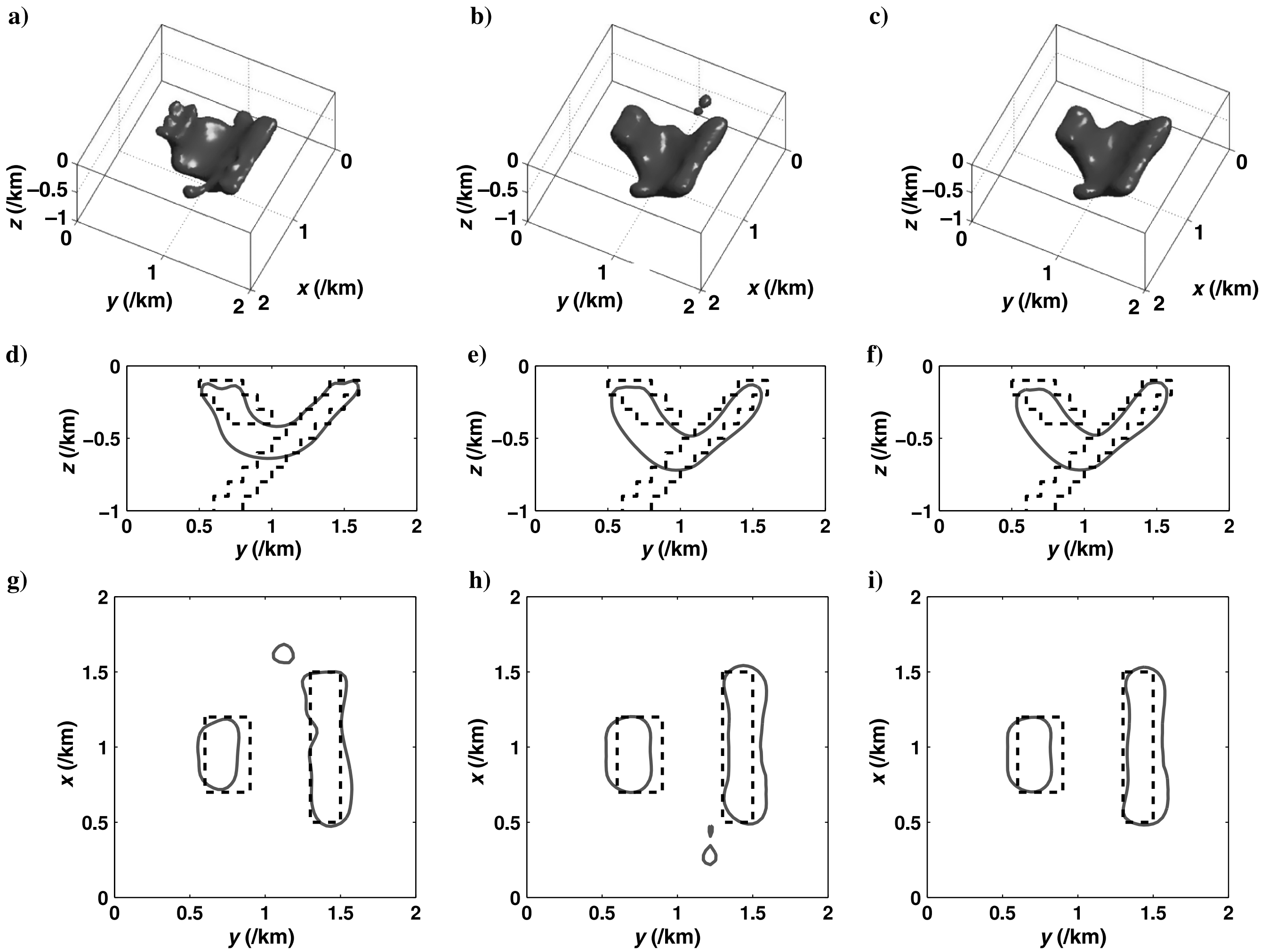

Figure 18. Two dikes: Shapes of numerical solutions at the 2000th iteration for $\rho = 1.0\ \mathrm{g/cm^3}$ with a one-sphere initial guess for different index sets; (a) $\mathbf{M} = \{xy, \Delta\}$, (b) $\mathbf{M} = \{zz\}$, (c) $\mathbf{M} = \{xy, \Delta, zz\}$, (d-f) cross sections of the numerical solutions in (a-c) at $x = 1$ km, and (g-i) cross sections of the numerical solutions in (a-c) at $z = -0.25$ km. Dashed lines indicate the true positions of the target.

we initialize the level-set function to be two well-separated spheres of the same radius 0.1 km, centered at $(1.0, 0.7, -0.3)$ and $(1.0, 1.4, -0.3)$ km, respectively.

To apply the level-set algorithm, because the range of subsurface density contrasts is from $0.8\ \mathrm{g/cm^3}$ to $1.0\ \mathrm{g/cm^3}$, we consider three different values of ρ_0 taking $\rho_0 = 0.8\ \mathrm{g/cm^3}$, $\rho_0 = 0.9\ \mathrm{g/cm^3}$, and $\rho_0 = 1.0\ \mathrm{g/cm^3}$. We rediscretize the computational domain Ω into $65 \times 65 \times 33$ uniform mesh points with the same grid size $1/32$ km in all directions.

For the three index sets $\mathbf{M} = \{xy, \Delta\}$, $\mathbf{M} = \{zz\}$, and $\mathbf{M} = \{xy, \Delta, zz\}$, by the level-set algorithm we obtain numerical solutions at the 2000th iteration and their cross sections at $x = 1$ km and $z = -0.25$ km as shown in Figures 15–17, respectively. We can see that for all three different values of ρ_0, numerical solutions match with true models reasonably well and locate source bodies at their true depths.

To test the robustness of the level-set algorithm, we initialize the level-set function to be a single sphere of radius 0.1 km centered at $(1.0, 0.7, -0.3)$ km and then we compute numerical solutions for all three index sets $\mathbf{M} = \{xy, \Delta\}$, $\mathbf{M} = \{zz\}$, and $\mathbf{M} = \{xy, \Delta, zz\}$ with $\rho_0 = 1.0\ \mathrm{g/cm^3}$. Numerical solutions at 2000th iteration and their cross sections at $x = 1$ km and $z = -0.25$ km are shown in Figure 18, in which dashed lines indicate the true positions of the source bodies. We can see that although the level-set algorithm fails in resolving source bodies, cross sections shown in Figures 18d–18i indicate that numerical solutions locate the true positions of source bodies.

CONCLUSION

We propose a local level-set method for the inversion of gravity-gradient data. Assuming that a homogeneous density contrast distribution with the value of the density contrast specified a priori is supported on an unknown bounded domain D, we were able to convert the original inverse problem into a domain inverse problem so that the level-set method can be applied to parametrize the unknown domain. We apply the migration method and a weighted L^1-regularization method to locate gravity centers of source bodies, which may provide robust initialization for the level-set algorithm. We also develop a low-rank-matrix decomposition algorithm to rapidly compute the mismatch and the Fréchet derivative. Extensive numerical experiments illustrate the effectiveness of the local level-set method.

ACKNOWLEDGMENTS

We thank the assistant editor J. Shragge, the associate editor X. Li, G. Barnes, C. Farquharson, and two anonymous reviewers for their many constructive and valuable comments and suggestions. J. Qian is supported by NSF-1222368.

REFERENCES

Barnes, G. J., and J. Barraud, 2012, Imaging geologic surfaces by inverting gravity gradient data with depth horizons: Geophysics, **77**, no. 1, G1–G11, doi: 10.1190/geo2011-0149.1.
Barnes, G. J., J. Barraud, J. Lumley, and M. Davies, 2008, Advantages of multi-tensor, high resolution gravity gradient data: 78th Annual International Meeting, SEG, Expanded Abstracts, 3587–3590.
Ben Hadj Miled, M. K., and E. L. Miller, 2007, A projection-based level-set approach to enhance conductivity anomaly reconstruction in electrical resistance tomography: Inverse Problems, **23**, 2375–2400, doi: 10.1088/0266-5611/23/6/007.
Brezis, H., 1974, Solutions with compact support of variational inequalities, dedicated to the memory of I. G. Petrovski: Uspekhi Matematicheskikh Nauk, **29**, 103–108.
Burger, M., 2001, A level set method for inverse problems: Inverse Problems, **17**, 1327–1356, doi: 10.1088/0266-5611/17/5/307.
Burger, M., and S. Osher, 2005, A survey on level set methods for inverse problems and optimal design: European Journal of Applied Mathematics, **16**, 263–301, doi: 10.1017/S0956792505006182.
Cecil, T., S. J. Osher, and J. Qian, 2006, Simplex free adaptive tree fast sweeping and evolution methods for solving level set equations in arbitrary dimension: Journal of Computational Physics, **213**, 458–473, doi: 10.1016/j.jcp.2005.08.020.
Cella, F., and M. Fedi, 2012, Inversion of potential field data using the structural index as weighting function rate decay: Geophysical Prospecting, **60**, 313–336, doi: 10.1111/j.1365-2478.2011.00974.x.
Condi, F., and M. Talwani, 1999, Resolution and efficient inversion of gravity gradiometry: 70th Annual International Meeting, SEG, Expanded Abstracts, 358–361.
Dorn, O., and D. Lesselier, 2006, Level set methods for inverse scattering: Inverse Problems, **22**, R67–R131, doi: 10.1088/0266-5611/22/4/R01.
Farquharson, C. G., and C. R. W. Mosher, 2009, Three-dimensional modelling of gravity data using finite differences: Journal of Applied Geophysics, **68**, 417–422, doi: 10.1016/j.jappgeo.2009.03.007.
Fedi, M., 2007, DEXP: A fast method to determine the depth and the structural index of potential fields sources: Geophysics, **72**, no. 1, I1–I11, doi: 10.1190/1.2399452.
Fedi, M., and G. Florio, 2006, SCALFUN: 3D analysis of potential field scaling function to determine independently or simultaneously structural index and depth to source: 77th Annual International Meeting, SEG, Expanded Abstracts, 963–967.
Fedi, M., and M. Pilkington, 2012, Understanding imaging methods for potential field data: Geophysics, **77**, no. 1, G13–G24, doi: 10.1190/geo2011-0078.1.
Fullagar, P., and G. Pears, 2010, From gravity gradient to density gradient: Abstracts from the ASEG-PESA Airbone Gravity Workshop, Geoscience Australia, Record 2010/23, 79–86.
Hou, S., K. Solna, and H.-K. Zhao, 2004, Imaging of location and geometry for extended targets using the response matrix: Journal of Computational Physics, **199**, 317–338, doi: 10.1016/j.jcp.2004.02.010.
Isakov, V., S. Leung, and J. Qian, 2011, A fast local level set method for inverse gravimetry: Communications in Computational Physics, **10**, 1044–1070, doi: 10.4208/cicp.100710.021210a.
Isakov, V., S. Leung, and J. Qian, 2013, A three-dimensional inverse gravimetry problem for ice with snow caps: Inverse Problems and Imaging, **7**, 523–544, doi: 10.3934/ipi.2013.7.523.
Jorgensen, G., and J. Kisabeth, 2000, Joint 3D inversion of gravity, magnetic and tensor gravity fields for imaging salt formations in the deepwater Gulf of Mexico: 71st Annual International Meeting, SEG, Expanded Abstracts, 424–426.
Koh, K., S. Kim, and S. Boyd, 2007, l1_ls: A Matlab solver for large-scale l1–regularized least squares problems., http://www.stanford.edu/~boyd/l1_ls/, accessed 12 September 2013.
Krahenbuhl, R., and Y. Li, 2006, Inversion of gravity data using a binary formulation: Geophysical Journal International, **167**, 543–556, doi: 10.1111/j.1365-246X.2006.03179.x.
Last, B. J., and K. Kubik, 1983, Compact gravity inversion: Geophysics, **48**, 713–721, doi: 10.1190/1.1441501.
Lee, J. B., 2001, FALCON gravity gradiometer technology: Exploration Geophysics, **32**, 247–250, doi: 10.1071/EG01247.
Leung, S., J. Qian, and R. Burridge, 2007, Eulerian Gaussian beams for high frequency wave propagation: Geophysics, **72**, no. 5, SM61–SM76, doi: 10.1190/1.2752136.
Leung, S., J. Qian, and S. J. Osher, 2004, A level set method for three dimensional paraxial geometrical optics with multiple sources: Communications in Mathematical Sciences, **2**, 643–672, doi: 10.4310/CMS.2004.v2.n4.a5.
Li, W., and S. Leung, 2013, A fast local level set based adjoint state method for first arrival transmission traveltime tomography with discontinuous slowness: Geophysical Journal International, **195**, 582–596, doi: 10.1093/gji/ggt244.
Li, W., S. Leung, and J. Qian, 2014, A level set-adjoint state method for crosswell transmission-reflection traveltime tomography: Geophysical Journal International, **199**, 348–367, doi: 10.1093/gji/ggu262.
Li, X., 2010, Efficient 3D gravity and magnetic modeling: Presented at the Electromagnetic, Gravity, and Magnetic (EGM) Methods International Workshop, EAGE, Extended Abstracts.
Li, Y., 2001a, 3D inversion of gravity gradiometer data: 72nd Annual International Meeting, SEG, Expanded Abstracts, 1470–1473.
Li, Y., 2001b, Processing gravity gradiometer data using an equivalent source technique: 72nd Annual International Meeting, SEG, Expanded Abstracts, 1466–1469.

Li, Y., and D. Oldenburg, 1998, 3D inversion of gravity data: Geophysics, **63**, 109–119, doi: 10.1190/1.1444302.
Li, Y., and D. Oldenburg, 2003, Fast inversion of large-scale magnetic data using wavelet transforms and a logarithmic barrier method: Geophysical Journal International, **152**, 251–265, doi: 10.1046/j.1365-246X.2003.01766.x.
Litman, A., D. Lesselier, and F. Santosa, 1998, Reconstruction of a 2-D binary obstacle by controlled evolution of a level-set: Inverse Problems, **14**, 685–706, doi: 10.1088/0266-5611/14/3/018.
Martinez, C., Y. Li, R. Krahenbuhl, and M. A. Braga, 2010, 3D inversion of airborne gravity gradiometry for iron ore exploration in Brazil: 80th Annual International Meeting, SEG, Expanded Abstracts, 1753–1757.
Martinez, C., Y. Li, R. Krahenbuhl, and M. A. Braga, 2013, 3D inversion of airborne gravity gradiometry data in mineral exploration: A case study in the Quadrilatero Ferrifero, Brazil: Geophysics, **78**, no. 1, B1–B11, doi: 10.1190/geo2012-0106.1.
Osher, S. J., and J. A. Sethian, 1988, Fronts propagating with curvature dependent speed: Algorithms based on Hamilton-Jacobi formulations: Journal of Computational Physics, **79**, 12–49, doi: 10.1016/0021-9991(88)90002-2.
Ozolins, V., R. Lai, R. Caflisch, and S. Osher, 2013, Compressed modes for variational problems in mathematics and physics: Proceedings of the National Academy of Sciences of the United States of America, **110**, 18368–18373, doi: 10.1073/pnas.1318679110.
Papadopoulos, D., M. Herty, V. Rath, and M. Behr, 2011, Identification of uncertainties in the shape of geophysical objects with level sets and the adjoint method: Computational Geosciences, **15**, 737–753, doi: 10.1007/s10596-011-9242-6.
Pilkington, M., 2012, Analysis of gravity gradiometer inverse problems using optimal design measures: Geophysics, **77**, no. 2, G25–G31, doi: 10.1190/geo2011-0317.1.
Portniaguine, O., and M. Zhdanov, 1999, Focusing geophysical inversion images: Geophysics, **64**, 874–887, doi: 10.1190/1.1444596.
Qian, J., L.-T. Cheng, and S. J. Osher, 2003, A level set based Eulerian approach for anisotropic wave propagations: Wave Motion, **37**, 365–379, doi: 10.1016/S0165-2125(02)00101-4.
Qian, J., and S. Leung, 2004, A level set method for paraxial multivalued traveltimes: Journal of Computational Physics, **197**, 711–736, doi: 10.1016/j.jcp.2003.12.017.
Qian, J., and S. Leung, 2006, A local level set method for paraxial multivalued geometric optics: SIAM Journal on Scientific Computing, **28**, 206–223, doi: 10.1137/030601673.
Qian, J., and W. W. Symes, 2002a, Adaptive finite difference method for traveltime and amplitude: Geophysics, **67**, 167–176, doi: 10.1190/1.1451472.
Qian, J., and W. W. Symes, 2002b, Finite-difference quasi-P traveltimes for anisotropic media: Geophysics, **67**, 147–155, doi: 10.1190/1.1451438.
Routh, P., G. Jorgensen, and J. Kisabeth, 2001, Base of the salt imaging using gravity and tensor gravity data: 72nd Annual International Meeting, SEG, Expanded Abstracts, 1482–1484.
Santosa, F., 1996, A level-set approach for inverse problems involving obstacles: ESAIM: Control, Optimisation and Calculus of Variations, **1**, 17–33, doi: 10.1051/cocv:1996101.
Sussman, M., P. Smereka, and S. J. Osher, 1994, A level set approach for computing solutions to incompressible two-phase flows: Journal of Computational Physics, **114**, 146–159, doi: 10.1006/jcph.1994.1155.
Van den Doel, K., U. Ascher, and A. Leitao, 2010, Multiple level sets for piecewise constant surface reconstruction in highly ill-posed problems: Journal of Scientific Computing, **43**, 44–66, doi: 10.1007/s10915-009-9341-x.
Zhao, H.-K., T. Chan, B. Merriman, and S. J. Osher, 1996, A variational level set approach for multiphase motion: Journal of Computational Physics, **127**, 179–195, doi: 10.1006/jcph.1996.0167.
Zhdanov, M., R. Ellis, and S. Mukherjee, 2004, Three dimensional regularized focusing inversion of gravity gradient tensor component data: Geophysics, **69**, 925–937, doi: 10.1190/1.1778236.
Zhdanov, M., X. Liu, G. Wilson, and L. Wan, 2011, Potential field migration for rapid imaging of gravity gradiometry data: Geophysical Prospecting, **59**, 1052–1071, doi: 10.1111/j.1365-2478.2011.01005.x.
Zheglova, P., C. G. Farquharson, and C. A. Hurich, 2013, 2D reconstruction of boundaries with level set inversion of traveltimes: Geophysical Journal International, **192**, 688–698, doi: 10.1093/gji/ggs035.